Atmospheric
Chemistry
and Physics
Discussions

1   # Retrieval of aerosol composition directly from
2   # satellite and ground-based measurements
3
4

5   Lei Li[1,2], Oleg Dubovik[2*], Yevgeny Derimian[2*], Gregory L Schuster[3], Tatyana
6   Lapyonok[2], Pavel Litvinov[4], Fabrice Ducos[2], David Fuertes[4], Cheng Chen[2],
7   Zhengqiang Li[5], Anton Lopatin[4], Benjamin Torres[2] , Huizheng Che[1]
8
9

10   [1]State Key Laboratory of Severe Weather (LASW) and Institute of Atmospheric
11   Composition, Chinese Academy of Meteorological Sciences, CMA, Beijing, 100081, China
12   [2]Univ. Lille, CNRS, UMR 8518 - LOA - Laboratoire d'Optique Atmosphérique, F-59000
13   Lille, France
14   [3]NASA Langley Research Center, Hampton, VA, USA
15   [4]GRASP-SAS, Remote Sensing Developments, Cité Scientifique, Univ. Lille, Villeneuve
16   d'Ascq, 59655, France
17   [5]State Environmental Protection Key Laboratory of Satellite Remote Sensing, Institute of
18   Remote Sensing and Digital Earth, Chinese Academy of Sciences, Beijing 100101, China
19
20
21   Correspondence to:
22   O. Dubovik (**oleg.dubovik@univ-lille.fr**);
23   Y. Derimian (**yevgeny.derimian@univ-lille.fr**)
24
25
26
27
28
29

30   ## Abstract

31   This study presents a novel methodology for remote monitoring of aerosol
32   composition over large spatial and temporal domains. The concept is realized within
33   the GRASP (Generalized Retrieval of Aerosol and Surface Properties) algorithm to
34   directly infer aerosol composition from the measured radiances. This approach is
35   different from the conventional methods that use post-processing of the retrieved
36   aerosol optical properties for aerosol typing. The proposed method assumes observed
37   aerosols as mixtures of particles composed of black carbon, brown carbon, absorbing
38   insoluble, non-absorbing insoluble embedded in a soluble host. The algorithm then
39   derives size distribution and the fractions of these components. The complex
40   refractive index of each component is fixed a priori and the complex refractive index
41   of mixture is computed using mixing rules. The approach is first tested with synthetic
42   data and the uncertainties are estimated. Then, it is applied to the real ground-based
43   AERONET and space-borne POLDER/PARASOL observations, known to be

Atmospheric
Chemistry
and Physics
Discussions

44   sensitive to aerosol complex refractive index. The study presents a first attempt to
45   derive aerosol composition from satellites. The obtained aerosol optical
46   characteristics are highly consistent with the standard products (R of ~ 0.9 for aerosol
47   optical thickness). The approach also presented an ability to separate between aerosol
48   properties in fine and coarse size fractions, in case of POLDER/PARASOL and
49   AERONET. Examples of application to POLDER/PARASOL on the global scale are
50   presented. The obtained spatial and temporal patterns of the aerosol composition
51   agree well with our knowledge on aerosol sources and transport features. Finally,
52   limitations and perspectives are discussed.
53

54   1 Introduction

55   Information about atmospheric aerosol chemical composition has a great
56   importance for monitoring and understanding of various aspects of climate and
57   environment. This information can be obtained by laboratory analysis of sampled
58   aerosol. However, the in-situ measurements require considerable effort and represent
59   only small areas without providing results on wide spatial and temporal scale. It is
60   known that chemical transport models are able to represent chemical component
61   concentrations with wide spatial and temporal coverage, and this capability has been
62   developed rapidly in the past decade. However, the models can have uncertainties
63   because they are initialized by gridded emission inventories that presently have
64   substantial uncertainties. For example, the carbon emissions inventories can be
65   uncertain with a factor of two, and this uncertainty is carried forward to the model
66   output (Bond et al., 1998; Cooke et al., 1999; Streets et al., 2001).
67   Aerosol components are often divided into two categories: strongly light-absorbing
68   components and mainly scattering (non-absorbing) components. The radiative
69   impacts of aerosols at the top of the atmosphere can change from cooling for highly
70   scattering aerosols to warming for highly absorbing aerosols located above highly
71   reflective surfaces like snow or clouds (Haywood and Shine, 1995). There are two
72   kinds of absorbing aerosols that are commonly found in the atmosphere: absorbing
73   carbon and mineral dust that contains iron oxides (Sokolik and Toon, 1999).
74   Light-absorbing carbon is composed of soot carbon and brown carbon (Andreae
75   and Gelencsér, 2006). Light-absorbing carbon is produced by incomplete combustion,
76   and it is an important component of atmospheric aerosol. The complex refractive
77   index of light-absorbing carbon is dependent upon the type of the fuel and the
78   conditions of combustion. Based on the origin of the material, combustion conditions,
79   morphological characteristics, chemical composition and optical properties (Andreae
80   and Gelencsér, 2006; Schkolnik et al., 2007), the term black carbon (BC), associated
81   with elemental carbon or soot, is used to define the strongly light-absorbing carbon in
82   the atmosphere. Meanwhile, the term brown carbon (BrC) is used for strongly
83   wavelength-dependent light-absorbing carbon particles whose absorption is greater at
84   near-ultraviolet and blue wavelengths (Chen and Bond, 2010; Dinar et al., 2007;
85   Hoffer et al., 2006; Jacobson, 1999; Kanakidou et al., 2005; Kirchstetter et al., 2004;
86   Schnaiter et al., 2006; Sun et al., 2007).

Atmospheric
Chemistry
and Physics
Discussions

87   Mineral dust particles can have a strong spectral signature, with strong absorption
88   at the UV and blue wavelengths when iron oxides are present. Hematite and goethite
89   are different forms of free iron, and they typically appear together (Arimoto et al.,
90   2002; Formenti et al., 2014; Lafon et al., 2006; Shi et al., 2012). The presence of iron
91   in mineral dust particles is known to be important for its biogeochemical and radiative
92   impacts (Jickells et al., 2005; Mahowald et al., 2005; Sokolik and Toon, 1999).
93   Although the regional distribution of the iron concentration is important for climate
94   studies, it is difficult to obtain since it requires in-situ aerosol sampling or simulation
95   of complex natural processes. In addition, mineral dust particles can be affected by
96   the presence of anthropogenic aerosol particles (e.g. carbonaceous particles produced
97   from biomass burning). Separating the absorption associated with light-absorbing
98   carbon from the absorption associated with mineral dust (especially iron oxides) is not
99   an evident task (Derimian et al., 2008) and determination of the relative proportions
100   of BC, BrC and iron oxides should consider differences in absorption spectral
101   dependence. For instance, Dubovik et al. (2002a) showed that the spectral absorption
102   of carbonaceous aerosol is distinct from that of mineral dust. Schuster et al. (2005)
103   inferred the BC column content from AERONET retrievals by assuming BC is the
104   source of all significant aerosol absorption in the AERONET retrievals. Koven and
105   Fung (2006) retrieved hematite concentration at dust sites based on the spectral
106   variability of the imaginary refractive index, while Arola et al. (2011) retrieved BrC
107   from AERONET retrievals. Wang et al. (2013) have added single-scatter albedo as an
108   additional constraint to the approach using refractive index (Arola et al., 2011;
109   Schuster et al., 2005) and made it feasible to distinguish BC, BrC and dust
110   simultaneously. Similarly, Li et al. (2015, 2013) investigate the microphysical, optical
111   and chemical properties of atmospheric aerosols by fitting the AERONET complex
112   refractive indices measured at Beijing and Kanpur. Recently, Schuster et al. (2016)
113   have used the AERONET size distributions and complex refractive indices to retrieve
114   the relative proportion of carbonaceous aerosols (BC and BrC) and free iron minerals
115   (hematite and goethite) in fine and coarse modes particles. Nevertheless, all above
116   remote sensing methods (Arola et al., 2011; Koven and Fung, 2006; Li et al., 2015,
117   2013; Schuster et al., 2016, 2009, 2005; Wang et al., 2013) that retrieve aerosol
118   composition relying on an intermediate retrieval of the refractive index (e.g. one
119   provided by the AERONET operational inversion). We also note that these retrievals
120   of aerosol composition are only conducted for ground-based remote sensing
121   measurements.
122   Global satellite observations of aerosol properties provide an opportunity to
123   validate and constrain the model simulations at large spatial and temporal scales
124   (Collins et al., 2001; Liu et al., 2005; Yu et al., 2006, 2004, 2003; Zhang et al.,
125   2008a). The integration of observations with model results can fill gaps in satellite
126   retrievals and constrain global distributions of aerosol properties to have good
127   agreement with ground-based measurements (Liu et al., 2005; Yu et al., 2006, 2003).
128   In this regard, inverse modeling can be used to reduce large aerosol simulation
129   uncertainties. For instance, several studies (Chen et al., 2018; Dubovik et al., 2008;
130   Henze et al., 2007) showed the ability to retrieve global aerosol sources with inverse

131   models that rely upon satellite observations. Therefore, the practice of satellite data
132   fusion into models provides a possibility of improving aerosol simulations of the pre-
133   and post-satellite eras. However, besides the knowledge of amounts (concentrations)
134   and locations of aerosol emissions, an accurate modeling of atmospheric aerosols and
135   their effects also requires information about particle composition. The lack of
136   comprehensive datasets providing multiple constraints for the key parameters
137   employed in the models has hindered the improvement of model simulation.
138   Specifically, improving the ability of aerosol composition estimation will require
139   enhancement of remote sensing capabilities to provide the aerosol composition
140   information on the global scale. The accuracy and specification of the aerosol
141   composition as retrieved from satellite observations should respond to the
142   requirements of the chemical transport models. At the same time, the information
143   content of remote sensing is limited and the main challenge is to identify the aerosol
144   composition parameters that can be successfully retrieved by remote sensing
145   measurements, given their sensitivity to the aerosol optical properties and complex
146   refractive index in particular.
147   The POLDER space instrument (Deschamps et al., 1994; Tanré et al., 2011) is an
148   example of the instrument providing satellite observations that are sensitive to aerosol
149   composition. The implementation of multi-wavelength, multi-angle and polarization
150   measurement capabilities has made it possible to derive particle properties (size,
151   shape and absorption; Dubovik et al., 2011; Waquet et al., 2013) that are essential for
152   characterizing and estimating aerosol composition. This study presents a methodology
153   for the direct retrieval of aerosol composition from such measurements. Our
154   methodology is stimulated by the Schuster et al. (2016, 2009, 2005) works on
155   deriving aerosol composition information from ground-based Sun/sky photometers of
156   the AERONET network. Here, the idea of the approach has evolved and expanded for
157   retrieving the aerosol composition from satellite remote sensing observations as well.
158   Namely, we have incorporated an aerosol composition module into the Generalized
159   Retrieval of Aerosol and Surface Properties (GRASP) algorithm (Dubovik et al.,
160   2014, 2011). It should be noted that GRASP is a versatile algorithm designed to
161   retrieve an extended set of atmospheric parameters from diverse remote sensing data,
162   including surface, airborne, and satellite observations. Here, we apply GRASP to both
163   ground- and space-based observations, with primary objective to develop an approach
164   for monitoring aerosol composition with extensive spatial and temporal coverage.
165   The objective of our GRASP/Composition approach is to retrieve the aerosol
166   composition directly from remote sensing measurements without intermediate
167   retrieval of the complex refractive index, as in previous studies (Arola et al., 2011;
168   Koven and Fung, 2006; Li et al., 2015, 2013; Schuster et al., 2016, 2009, 2005; Wang
169   et al., 2013). This new approach has a more direct link to the measured radiance field
170   than the "intermediate" approaches, and we therefore expect a reduction in the
171   retrieval uncertainties. The GRASP/Composition approach also suggests an additional
172   constraint on the refractive index spectral variability that is not employed in the
173   conventional retrieval algorithms. Specifically the spectral variability of aerosol
174   complex refractive index is constrained in the GRASP/Composition retrieval by the

175 spectral dependences of the aerosol species used in the algorithm. It is expected that
176 such constraints can improve the retrievals in various situations.
177   One of the principal difficulties, however, is the identification of an adequate
178 conversion model for linking refractive index to aerosol composition. An ideal
179 conversion model should cover the entire range of aerosol complex refractive indices
180 and also provide a unique connection between spectral refractive index and aerosol
181 composition. Therefore, our primary objective focuses on identifying the optimal
182 transformation of chemical and physical aerosol information to optical properties (e.g.
183 refractive index). Once developed, the efficiency of the concept is verified and
184 demonstrated by applying GRASP/Composition to ground-based Sun/sky photometric
185 measurements, since this type of measurement usually presents a higher sensitivity to
186 aerosol absorption than the satellite remote sensing. Finally, the outcome of the
187 GRASP/Composition approach is demonstrated with the application of the aerosol
188 composition retrieval to multi-angular polarimetric POLDER/PARASOL satellite
189 observations.
190

2 Methodology

192   GRASP is a highly rigorous and versatile aerosol and surface reflectance retrieval
193 algorithm that is accessible at https://www.grasp-open.com (Dubovik et al., 2014,
194 2011). The essence of methodological developments in this study is to integrate a new
195 conversion model designed to link aerosol composition with optical and
196 microphysical characteristics into the standard GRASP inversion procedure. The
197 general logistics is shown in Fig. 1 (modified from (Dubovik et al., 2011)). The
198 algorithm is divided into several interacting but rather independent modules to
199 enhance its flexibility. The straightforward exchange of limited parameters minimizes
200 the interactions between the modules. The "Forward Model" and "Numerical
201 Inversion" are the two most complex and elaborate modules in the algorithm. The
202 "Forward Model" is developed in a quite universal way to quantitatively simulate the
203 measured atmospheric radiation with given surface and aerosol properties. The
204 "Numerical Inversion" module (which can be used in various applications, some not
205 even related to atmospheric remote sensing) includes general mathematical operations
206 unrelated to the particular physical nature of the observations. Numerical inversion is
207 implemented as a statistically optimized fitting of observations based upon the multi-
208 term least squares method (LSM), and combines the advantages of a variety of
209 approaches. The module provides transparency and flexibility for developing
210 algorithms that invert passive or active observations to derive several groups of
211 unknown parameters (Dubovik, 2004).
212   As a consequence of such organization of the algorithm, it can equally be applied
213 (with minimal changes) to invert observations from different satellite sensors or
214 ground-based instruments (Benavent-oltra et al., 2017; Espinosa et al., 2017; Lopatin
215 et al., 2013; Román et al., 2018, 2017; Tsekeri et al., 2017). A full description of the
216 "Forward Model" and "Numerical Inversion" algorithm modules can be found in
217 Dubovik et al. (2011). The following sections provide a description of the

Atmospheric
Chemistry
and Physics
Discussions

Open Access

218 modifications conducted for realization of the GRASP/Composition approach
219 (schematically presented by red dashed frames in Fig. 1).
220

221 **2.1 Forward model**

222

223   The formulation of the forward radiative transfer modeling in the presented
224 approach is generally similar to the formulation of the standard GRASP algorithm
225 where the modeling of the aerosol scattering matrices has been implemented
226 following the ideas described in Dubovik and King (2000) and Dubovik et al. (2006,
227 2002b). However, we implemented some modifications in modeling of aerosol single
228 scattering. Namely, the real and imaginary parts of the aerosol complex refractive
229 index are calculated using fractions of aerosol composition elements and fixed
230 refractive index of these elements as assumed in the conversion model. Thus, the new
231 composition approach uses the same forward model as described in Dubovik et al.
232 (2011), except that aerosol component fractions are iterated in the vector of the
233 retrieved unknowns (instead of refractive index) and refractive index is computed a
234 posteriori.
235   It is worth noting that the aerosol properties in the GRASP algorithm are retrieved
236 simultaneously with the surface reflectance characteristics. The land surface
237 Bidirectional Reflectance Distribution Function (BRDF) in GRASP is described by
238 the kernel-driven Ross-Li model. This model uses a linear combination of three
239 kernels f_{iso}, f_{vol}, and f_{geom} representing isotropic, volumetric, and geometric optics
240 surface scattering, respectively (Li and Strahler, 1992; Roujean et al., 1992; Wanner
241 et al., 1995). The semi-empirical equation by Maignan et al. (2009) is used for the
242 Bidirectional Polarization Distribution Function (BPDF). The reflective properties of
243 ocean surface are modeled analogously to earlier POLDER algorithm developments
244 (Deuzé et al., 2001; Herman et al., 2005; Tanré et al., 2011). Fresnel reflection of the
245 agitated sea surface is taken into account using the Cox and Munk model (Cox and
246 Munk, 1954). The water leaving radiance is nearly isotropic (Voss et al., 2007) and
247 modeling shows that its polarization is negligible (Chami et al., 2001; Chowdhary et
248 al., 2006; Ota et al., 2010). The Fresnel term and the white cap reflection are taken
249 into account by Lambertian unpolarized reflectance. The whitecap reflectance is
250 driven by the wind speed at the sea surface according to the Koepke model (Koepke,
251 1984). The seawater reflectance at short wavelengths depends on the properties of
252 oceanic water and can be significant. Thus, in present model, the wind speed and the
253 magnitude of seawater reflectance at each wavelength are retrieved simultaneously
254 with the atmospheric aerosol properties.
255   The aerosol and surface characteristics are determined by parameters included in
256 the vector of unknowns and correspondingly they are inferred from observations.
257 Table 1 shows the list of measurements and retrieved parameters from
258 POLDER/PARASOL observations. For AERONET retrieval the list of parameters is
259 not shown here. However, in principle, it is analogous to POLDER/PARASOL, with

Atmospheric
Chemistry
and Physics
Discussions

260   the difference that the set of observations is different (i.e. AERONET uses AOT and
261   transmitted total radiances at different wavelengths) and that surface parameters are
262   not retrieved but fixed from the climatology.
263

264   **2.2 Numerical inversion**

265   The numerical inversion implemented in this study follows the methodology
266   described in the paper of Dubovik et al. (2011). The only difference is that the
267   GRASP/Composition approach retrieves the fractions of different aerosol components
268   instead of the spectral dependence of the complex refractive index. Therefore, this
269   section describes only the modifications that are needed to implement the
270   GRASP/Composition approach.
271   GRASP retrieval is designed as a statistically optimized fitting routine and uses
272   multiple a priori constraints. GRASP can implement two different scenarios of
273   satellite retrievals: (i) conventional single-pixel retrieval for processing of satellite
274   images pixel by pixel and (ii) multiple-pixel retrieval for inverting a large group of
275   pixels   simultaneously.   The   multi-pixel   approach   can   be   used   for
276   POLDER/PARASOL data for improving consistency of temporal and spatial
277   variability of retrieved characteristic. The main modifications required for the
278   composition approach are related to the definition of a priori constraints.
279   Correspondingly, two types of a priori constraints are reformulated in the composition
280   retrieval approach: constraints for single pixel and constraints limiting inter-pixel
281   variability of derived parameters.

282   **2.2.1 Single-pixel observation fitting**

283   For each i-th pixel, the retrieval follows a multi-term LSM fitting of joint sets of
284   data combining the observations with a priori constraints defined by the system of
285   equations $\boldsymbol{f}_i^* = \boldsymbol{f}_i(\boldsymbol{a}_i) + \Delta\boldsymbol{f}_i$:
286

287
$$\begin{cases} \boldsymbol{f}_i^* = \boldsymbol{f}_i(\boldsymbol{a}) + \Delta\boldsymbol{f}_i \\ 0_i^* = \boldsymbol{S}_i\boldsymbol{a}_i + \Delta(\Delta\boldsymbol{a}_i) \Rightarrow \boldsymbol{f}_i^* = \boldsymbol{f}_i(\boldsymbol{a}_i) + \Delta\boldsymbol{f}_i \\ \boldsymbol{a}_i^* = \boldsymbol{a}_i + \Delta\boldsymbol{a}_i^* \end{cases} \quad (1)$$

288

289   Here, $\boldsymbol{f}_i^*$ denotes a vector of the measurements, $\Delta\boldsymbol{f}_i^*$ denotes a vector of
290   measurement uncertainties, $\boldsymbol{a}_i$ denotes a vector of unknowns in i-th pixel. The second
291   expression in Eq. (1) characterizes the a priori smoothness assumptions that constrain
292   the variability of the size distributions and the spectral dependencies of the retrieved
293   surface reflectance parameters. The matrix S includes the coefficients for calculating
294   the m-th differences of $dV(r_j)/dlnr$, $Frac(i)$, $f_{iso}(\lambda_i)$, $f_{vol}(\lambda_i)$, and $f_{geom}(\lambda_i)$. The
295   m-th differences are numerical equivalents of the m-th derivatives. 0_i^* represents
296   vector of zeros and $\Delta(\Delta\boldsymbol{a})$ represents vector of the uncertainties that characterizes the
297   deviations of the differences from the zeros. This equation indicates that all of these
298   m-th differences are equal to zeros within the uncertainties $\Delta(\Delta\boldsymbol{a}_i)$. The third

299   expression in Eq. (1) includes the vector of a priori estimates $\boldsymbol{a}_i^*$, as well as the vector
300   of the uncertainties ($\Delta \boldsymbol{a}_i^*$) in a priori estimates of the i-th pixel.
301   The statistically optimized solution of Eq. (1) corresponds to the minimum of the
302   following quadratic form (according to multi-term LSM):
303

$$\Psi_i(\boldsymbol{a}_i) = \Psi_f(\boldsymbol{a}_i) + \Psi_\Delta(\boldsymbol{a}_i) + \Psi_a(\boldsymbol{a}_i)$$

304

305   $$= \frac{1}{2}((\Delta \boldsymbol{f}^P)^T (\boldsymbol{W}_f)^{-1} \Delta \boldsymbol{f}^P + \gamma_\Delta (\boldsymbol{a}_i)^T \Omega \boldsymbol{a}_i + \gamma_a (\boldsymbol{a}_i - \boldsymbol{a}_i^*)^T \boldsymbol{W}_a^{-1} (\boldsymbol{a}_i - \boldsymbol{a}_i^*)). \quad (2)$$

306

307   Following Dubovik et al. (2011), all equations are expressed with weighting
308   matrices W that are defined as $\boldsymbol{W} = (1/\varepsilon^2)\boldsymbol{C}$ (dividing the corresponding covariance
309   matrix C by its first diagonal element ε^2); the Lagrange multipliers γ_a and γ_Δ are
310   written as $\gamma_\Delta = \varepsilon_f^2/\varepsilon_\Delta^2$ and $\gamma_a = \varepsilon_f^2/\varepsilon_a^2$, where $\varepsilon_f^2, \varepsilon_\Delta^2$, and ε_a^2 represent the first
311   diagonal elements of corresponding covariance matrices $\boldsymbol{C}_f$, $\boldsymbol{C}_\Delta$, and $\boldsymbol{C}_a$. Thus, in this
312   general formulation the component fractions ($Frac(i)$) of aerosol composition are
313   presented as unknowns instead of $n(\lambda_j)$ and $k(\lambda_j)$.
314

315   **2.2.2 Multiple-pixel observation fitting**

316   In this retrieval regime the fitting for a group of pixels is constrained by the extra a
317   priori limitations on inter-pixel variability of aerosol and/or surface reflectance
318   properties. Since the information content of the reflected radiation from a single pixel
319   is sometimes insufficient for a unique retrieval of all unknown parameters, the
320   presented approach can improve the stability of satellite data inversions (Dubovik et
321   al., 2011). The inversion of the multi-pixel observations is a solution for a combined
322   system of equations. For example, a three-pixel system can be defined as following:
323

324   $$\begin{cases} \boldsymbol{f}_1^* = \boldsymbol{f}_1(\boldsymbol{a}_1) + \Delta \boldsymbol{f}_1 \\ \boldsymbol{f}_2^* = \boldsymbol{f}_2(\boldsymbol{a}_2) + \Delta \boldsymbol{f}_2 \\ \boldsymbol{f}_3^* = \boldsymbol{f}_3(\boldsymbol{a}_3) + \Delta \boldsymbol{f}_3 \\ \quad \dots \\ \boldsymbol{0}_x^* = \boldsymbol{S}_x \boldsymbol{a} + \Delta(\Delta_x \boldsymbol{a}) \\ \boldsymbol{0}_y^* = \boldsymbol{S}_y \boldsymbol{a} + \Delta(\Delta_y \boldsymbol{a}) \\ \boldsymbol{0}_t^* = \boldsymbol{S}_t \boldsymbol{a} + \Delta(\Delta_t \boldsymbol{a}) \end{cases}, \quad (3)$$

325

326   where the subscript "i" (i=1, 2, 3, …) is the pixel index. The total vector of unknowns
327   a is combined by the vectors of unknowns $\boldsymbol{a}_i$ of each i-th pixel, i.e.
328    $\boldsymbol{a}^T = (\boldsymbol{a}_1; \boldsymbol{a}_2; \boldsymbol{a}_3)^T$. The matrices $\boldsymbol{S}_x$, $\boldsymbol{S}_y$ and $\boldsymbol{S}_t$ include the coefficients for
329   calculating the m-th differences of spatial or temporal inter-pixel variability for each
330   retrieved parameter a_k that characterizes $dV(r_j)/dlnr$, $Frac(i)$, $f_{iso}(\lambda_i)$, $f_{vol}(\lambda_i)$,
331   and $f_{geom}(\lambda_i)$. The vectors $\boldsymbol{0}_x^*$, $\boldsymbol{0}_y^*$, $\boldsymbol{0}_t^*$ denote vectors of zeros and the vectors
332    $\Delta(\Delta_x \boldsymbol{a})$, $\Delta(\Delta_y \boldsymbol{a})$ and $\Delta(\Delta_t \boldsymbol{a})$ denote vectors of the uncertainties characterizing the
333   deviations of the differences from the zeros.

334   The statistically optimized multi-term LSM solution corresponds to the minimum
335   of the following quadratic $\Psi(\boldsymbol{a}^P)$:

336

337 $$\Psi(\boldsymbol{a}^P) = \left(\sum_{i=1}^{N_{pixels}} \Psi_i(\boldsymbol{a}^P)\right) + \frac{1}{2}(\boldsymbol{a}^P)^T \boldsymbol{\Omega}_{inter}\boldsymbol{a}^P. \tag{4}$$

338   This is the sum of the corresponding single-pixel forms (first term) and an inter-pixel
339   smoothing component (2nd term). The smoothness matrix $\boldsymbol{\Omega}_{inter}$ in the inter-pixel
340   smoothing term is defined as:

341

342 $$\boldsymbol{\Omega}_{inter} = \gamma_x \boldsymbol{S}_x^T \boldsymbol{S}_x + \gamma_y \boldsymbol{S}_y^T \boldsymbol{S}_y + \gamma_t \boldsymbol{S}_t^T \boldsymbol{S}_t. \tag{5}$$

343

344   Hence, the solution of a multi-pixel system of N pixels is not equivalent to the
345   solution of N independent single pixel systems.

346

347   **2.2.3 A priori smoothness constraints of fitting**

348   For the framework of deriving aerosol composition from the POLDER/GRASP
349   retrieval, the vector $\boldsymbol{a}_i$ is composed as:

350

351 $$\boldsymbol{a} = (\boldsymbol{a}_v \boldsymbol{a}_{frac} \boldsymbol{a}_{sph} \boldsymbol{a}_{Vc} \boldsymbol{a}_h \boldsymbol{a}_{brdf,1} \boldsymbol{a}_{brdf,2} \boldsymbol{a}_{brdf,3} \boldsymbol{a}_{bpdf})^T, \tag{6}$$

352

353   where $\boldsymbol{a}_v$, $\boldsymbol{a}_{frac}$, and $\boldsymbol{a}_{sph}$ represent the constituents of the vector a corresponding to
354   $dV(r_i)/dlnr$, $Frac(i)$ and C_{sph}. Then $\boldsymbol{a}_h$ characterizes the mean altitude of the
355   aerosol layer h_a, the element $\boldsymbol{a}_{Vc}$ represents the total volume concentration, and $\boldsymbol{a}_v$
356   are the logarithms of $dV(r)/dlnr$ which are normalized by total volume
357   concentration. The three components ($\boldsymbol{a}_{brdf,1}, \boldsymbol{a}_{brdf,2}, \boldsymbol{a}_{brdf,3}$) are related to the
358   logarithms of the spectrally dependent parameters $k_{iso}(\lambda_i)$, $k_{vol}(\lambda_i)$ and $k_{geom}(\lambda_i)$
359   employed in Ross-Li model. The vector $\boldsymbol{a}_{bpdf}$ includes the parameters of the BPDF
360   model. Thus, this work differentiates from Dubovik et al. (2011) by retrieving the
361   volume fractions of the aerosol components (i.e. $Frac(i)$) instead of the complex
362   refractive index.
363   There is no evident connection between the retrieved fractions of aerosol
364   composition in each single pixel, so no smoothness constraints are used for $\boldsymbol{a}_{frac}$. The
365   matrix S for each i-th pixel is the same and has the following array structure (Dubovik
366   et al., 2011):

367

Atmospheric
Chemistry
and Physics
Discussions

368
$$Sa = \begin{pmatrix} S_v & 0 & 0 & 0 & 0 & 0 & 0 & 0 & 0 \\ 0 & 0 & 0 & 0 & 0 & 0 & 0 & 0 & 0 \\ 0 & 0 & 0 & 0 & 0 & 0 & 0 & 0 & 0 \\ 0 & 0 & 0 & 0 & 0 & 0 & 0 & 0 & 0 \\ 0 & 0 & 0 & 0 & 0 & 0 & 0 & 0 & 0 \\ 0 & 0 & 0 & 0 & S_{brdf,1} & 0 & 0 & 0 \\ 0 & 0 & 0 & 0 & 0 & S_{brdf,2} & 0 & 0 \\ 0 & 0 & 0 & 0 & 0 & 0 & S_{brdf,3} & 0 \\ 0 & 0 & 0 & 0 & 0 & 0 & 0 & S_{bpdf} \end{pmatrix} \begin{pmatrix} \boldsymbol{a}_v \\ a_{frac} \\ a_{sph} \\ a_{Vc} \\ a_h \\ \boldsymbol{a}_{brdf,1} \\ \boldsymbol{a}_{brdf,2} \\ \boldsymbol{a}_{brdf,3} \\ \boldsymbol{a}_{bpdf} \end{pmatrix}, \qquad (7)$$

369
370 where the corresponding matrices $S_{...}$ have different dimensions and describe
371 differences of different order. The vectors in Eq. (7) corresponding to $\boldsymbol{a}_{frac}$, $\boldsymbol{a}_{sph}$,
372 $\boldsymbol{a}_{Vc}$, $\boldsymbol{a}_h$ contain only zeros because no smoothness constraint can be applied to these
373 parameters. The errors $\Delta(\Delta\boldsymbol{a})$ are assumed independent for different components of
374 the vector $(\Delta\boldsymbol{a})^*$ and the smoothness matrix for each i-th pixel can be written as:
375

376
$$\gamma_\Delta\Omega = \begin{pmatrix} \gamma_{\Delta,1}\Omega_1 & 0 & 0 & 0 & 0 & 0 & 0 & 0 \\ 0 & 0 & 0 & 0 & 0 & 0 & 0 & 0 \\ 0 & 0 & 0 & 0 & 0 & 0 & 0 & 0 \\ 0 & 0 & 0 & 0 & 0 & 0 & 0 & 0 \\ 0 & 0 & 0 & 0 & 0 & 0 & 0 & 0 \\ 0 & 0 & 0 & 0 & \gamma_{\Delta,2}\Omega_2 & 0 & 0 & 0 \\ 0 & 0 & 0 & 0 & 0 & \gamma_{\Delta,3}\Omega_3 & 0 & 0 \\ 0 & 0 & 0 & 0 & 0 & 0 & \gamma_{\Delta,4}\Omega_4 & 0 \\ 0 & 0 & 0 & 0 & 0 & 0 & 0 & \gamma_{\Delta,5}\Omega_5 \end{pmatrix}, \qquad (8)$$

377
378 where $\boldsymbol{\Omega}_i = \boldsymbol{S}_i^T \boldsymbol{W}_i^{-1} \boldsymbol{S}_i$ uses the derivative matrices $\boldsymbol{S}_i$ (i=1, …, 5), $\boldsymbol{S}_v$, $\boldsymbol{S}_{brdf,1}$, $\boldsymbol{S}_{brdf,2}$,
379 $\boldsymbol{S}_{brdf,3}$, $\boldsymbol{S}_{bpdf}$.
380   The inter-pixel smoothing term given by Eq. (5) is defined in a very similar way as
381 described by Dubovik et al. (2011), and therefore it is not written here explicitly.
382 Indeed, the spatial and temporal variability of composition is very similar to the
383 variability of refractive index, since both depend only upon the variability of aerosol
384 type.
385   We note that the above equations apply to the POLDER/GRASP retrievals, but
386 corresponding equations are trivially obtained for the AERONET/GRASP retrievals
387 by excluding parameters describing surface reflectance and aerosol height.
388
389

390 ## 2.3 Model of optical properties of aerosol composition

391 ### 2.3.1 Definition and assumptions

392   The aerosol refractive index required for the forward calculations (see Fig. 1) is
393 derived by assuming a mixing model and employing fractions of aerosol species;
394 therefore, the retrieval of aerosol composition requires the selection of a mixing rule.
395 In our work, we decided to use a simple and widely tested Maxwell-Garnett effective

Atmospheric
Chemistry
and Physics
Discussions

396   medium approximation. Indeed, the choice of the mixing rule is of importance since it
397   can significantly affect the retrieval results. In order to get an idea about the influence
398   of the mixing rule choice, the retrievals were produced also using the volume
399   weighted mixing rule and the results are inter-compared.
400   The Maxwell-Garnett mixing rule has been extensively applied in many studies for
401   retrieval of aerosol composition from ground-based remote sensing measurements (Li
402   et al., 2015, 2013; Schuster et al., 2016, 2009, 2005; Wang et al., 2013). As Fig. 2
403   illustrates, the first step in the Maxwell-Garnett conversion model is the designation
404   of a "host" and calculation of the refractive index of the host. In general, the host can
405   be formed by water and soluble inorganic species (e.g. ammonium nitrite, ammonium
406   sulfate, sea salt). It is well known that inorganic salt particles are mostly hygroscopic
407   and deliquescence in humid air. The phase transition from a solid particle to a saline
408   droplet (host) usually occurs when the relative humidity reaches a specific value,
409   known as the deliquescence point, that is specific to the chemical composition of the
410   aerosol particle (Orr et al., 1958; Tang, 1976; Tang and Munkelwitz, 1993). The
411   refractive indices of hygroscopic aerosols change with the additional amount of water
412   that is absorbed in response to changing relative humidity. These changes in refractive
413   index, including also the changes in specific density, size and mass fraction, have
414   been accurately measured as functions of relative humidity (Tang, 1996; Tang and
415   Munkelwitz, 1994, 1991).
416   In the presented approach, the host is assumed to depend upon the properties and
417   proportions of ammonium nitrate and water (uncertainties due to selection of
418   ammonium nitrate are evaluated further on). The real refractive index (at the 0.6328
419   μm wavelength) for a host mixture of ammonium nitrate and water can be expressed
420   as

422        $n = 1.33 + (1.22 \times 10^{-3})X + (8.997 \times 10^{-7})X^2 + (1.666 \times 10^{-8})X^3,$ (9)

424   where X is the weight percent of ammonium nitrate (Tang and Munkelwitz, 1991).
425   Refractive indices at other wavelengths are spectrally interpolated utilizing
426   measured data (Downing and Williams, 1975; Gosse et al., 1997; Hale and Querry,
427   1973; Kou et al., 1993; Palmer and Williams, 1974; Tang, 1996; Tang and
428   Munkelwitz, 1991). A detailed description and FORTRAN subroutines for calculating
429   the host complex refractive index is accessible at the website of GACP (Global
430   Aerosol Climatology Project, https://gacp.giss.nasa.gov/data_sets/).
431   Once the refractive index of the host is determined, the refractive index of the
432   mixture is computed using the Maxwell-Garnett equations. The Maxwell-Garnett
433   effective medium approximation allows computation of the average dielectric
434   function based upon the average electric fields and polarizations of a host matrix with
435   embedded inclusions, and can model insoluble particles suspended in a solution
436   (Bohren and Huffman, 1983; Lesins et al., 2002).
437   The dielectric functions of aerosols are not typically tabulated in the literature, so
438   they must be computed from the refractive index. Once the dielectric functions are
439   known for the host and its constituents, the Maxwell-Garnett dielectric function for a

440 mixture can be calculated. For example, for two types of inclusions in a host, the
441 dielectric function of the mixture can be expressed as (Schuster et al., 2005):
442

$$\varepsilon_{MG} = \varepsilon_m \left[1 + \frac{3(f_1 \frac{\varepsilon_1 - \varepsilon_m}{\varepsilon_1 + 2\varepsilon_m} + f_2 \frac{\varepsilon_2 - \varepsilon_m}{\varepsilon_2 + 2\varepsilon_m})}{1 - f_1 \frac{\varepsilon_1 - \varepsilon_m}{\varepsilon_1 + 2\varepsilon_m} - f_2 \frac{\varepsilon_2 - \varepsilon_m}{\varepsilon_2 + 2\varepsilon_m}} \right], \tag{10}$$

444

445 where ϵ_m, ϵ_1, and ϵ_2 are the complex dielectric functions of the host matrix and
446 inclusions, and f_1, f_2 are the volume fractions of the inclusions. If we use the case of
447 $f_2 = 0$, the corresponding complex refractive index of the mixture can be obtained by
448 Eqs. (11) − (12):

$$m_r = \sqrt{\frac{\sqrt{\varepsilon_r^2 + \varepsilon_i^2} + \varepsilon_r}{2}}, \tag{11}$$

450

$$m_i = \sqrt{\frac{\sqrt{\varepsilon_r^2 + \varepsilon_i^2} - \varepsilon_r}{2}}, \tag{12}$$

452

453 where ε_r and ε_i denote the real and imaginary components of the mixture dielectric
454 function, ε_{MG}.

455   The selected refractive indices of inclusions in the Maxwell-Garnett effective
456 medium approximation model in this study are shown in Fig. 3. Figure 3 also
457 illustrates the assumption on the size resolved aerosol composition presented as an
458 additional constraint. Our selection of aerosol elements and the size resolved
459 composition results from the examination of a series of sensitivity tests and stability
460 of the inversion results. The size resolved composition formulation was chosen
461 because a similarity in spectral signatures of some aerosol species induced a difficulty
462 of their distinguishing in the considered in this study observational configurations.
463 For instance, brown carbon (BrC) and iron oxides (hematite and goethite) have
464 similar tendency in spectral absorption; that is, increasing the imaginary refractive
465 index towards ultraviolet wavelengths (Chen and Cahan, 1981; Chen and Bond, 2010;
466 Kerker et al., 1979; Schuster et al., 2016). At the same time, it is known that
467 carbonaceous absorbing aerosol particles dominate in the fine mode and mineral dust
468 absorption dominates in the coarse mode. Hence, black carbon (BC) and brown
469 carbon (BrC) are assumed to be the only absorbing insolubles in the fine mode and
470 iron oxides are assumed to be the only absorbing insolubles in the coarse mode. In
471 addition, the fine mode includes non-absorbing insoluble species (FNAI) that
472 represent fine dust or non-absorbing organic carbon (OC), non-absorbing soluble
473 species (FNAS) representing anthropogenic salts and aerosol water content (FAWC).
474 The coarse mode includes absorbing insoluble species (CAI), which are mainly iron
475 oxides, but can also include all other absorbing elements. The coarse mode also
476 includes non-absorbing insoluble (CNAI) species that mainly represent the bulk dust
477 material, but can be also non-absorbing insoluble organic carbon particles, non-

Atmospheric
Chemistry
and Physics
Discussions

478 absorbing soluble species (CNAS) representing anthropogenic or natural salts (e.g.
479 sea salts) and aerosol water content (CAWC). It should be clarified that refractive
480 index of only one element is used for each species; however, our tests confirmed that
481 some elements are indistinguishable from the optical point of view, at least for the
482 measurement configurations expected in the scope of the presented algorithm
483 applications. Thus, several of the assumed species in the mixing model elements can
484 be associated with different elements.

485

486 **2.3.2 Sensitivity tests**

487 Using the above modifications to the GRASP algorithm described in Dubovik et
488 al. (2011), the aerosol composition retrieval approach was tested for inversion of
489 ground-based AERONET and POLDER/PARASOL satellite observations. For
490 verification of the proposed concept and the algorithm performance, a series of
491 sensitivity tests were conducted using synthetic data. A comprehensive series of
492 sensitivity tests were mainly conducted with the POLDER/PARASOL observations
493 because, unlike the AERONET retrievals, sensitivity of POLDER/PARASOL
494 observations to aerosol complex refractive index has not been systematically
495 explored. Thus, first, the POLDER/PARASOL radiances and polarization
496 measurements were simulated using forward calculations. Then, the synthetic
497 measurements were inverted using the GRASP algorithm with the size-dependent
498 aerosol composition approach and the Maxwell-Garnett mixing model. The tests were
499 conducted for a range of aerosol composition fractions for the species described
500 above and a variety of observational configurations such as spectral channels, viewing
501 geometry etc. Figure 4 presents an example of the assumed and retrieved fractions of
502 aerosol species in fine and coarse modes. The statistics of the sensitivity test results
503 are presented in Table 2, where we compare assumed and retrieved aerosol
504 parameters (fractions of aerosol elements, aerosol optical thickness (AOT), Single
505 Scattering Albedo (SSA) and complex refractive index at 675 nm). The results for
506 other wavelengths are very similar to that presented at 675 nm. In all the conducted
507 tests, the results demonstrated that in frame of the designed model the use of the size-
508 dependent Maxwell-Garnett conversion model allows the algorithm to distinguish
509 amongst the assumed aerosol species, including ammonium nitrate and water in the
510 host.

511

512 **2.3.3 Uncertainty assessment**

513 An important range of variability exists in the literature-reported refractive indices
514 of the aerosol species. Different assumptions on the refractive index of an aerosol
515 species can result in different retrieved fractions of the species proposed in this study.
516 To evaluate a possible range of the retrieved fractions due to uncertain knowledge of
517 the refractive indexes and difficulty to select one representative value, a series of
518 supplementary calculations were conducted using a range of refractive indices found

Atmospheric
Chemistry
and Physics
Discussions
Open Access
EGU

519 in the literature. Figure 5 shows the refractive indices employed in the algorithm and
520 those used for the assessment of the uncertainties in the retrieved aerosol fractions.
521 The tests are conducted as follows: first, synthetic measurements are created by
522 forward calculations while employing the complex refractive index assumed in the
523 algorithm; second, another complex refractive index is used in the inversion
524 procedure while retrieving the fractions of the aerosol species from the synthetic
525 measurements. Thus, the comparison of the assumed in the forward calculations and
526 the retrieved in the inversion procedure aerosol species fractions provides an error
527 assessment due to possible variability of their complex refractive index. The
528 calculations were conducted for all aerosol species that are assumed be embedded in
529 the host of the Maxwell-Garnett effective medium approximation. In addition, the
530 tests are also conducted for different fractions of the elements and for different values
531 of AOT, reflecting sensitivity of the retrievals to varying aerosol loading.
532   An extensive review of BC refractive indices can be found in Bond and Bergstrom
533 (2006) where the recommended imaginary part is in range from 0.63 to 0.79 at visible
534 wavelengths. The spectrally invariant value of 0.79 was adopted in the previous
535 studies (Bond et al., 2013; Bond and Bergstrom, 2006). Based on this literature, we
536 use the spectrally invariant complex refractive index for BC of $1.95 + 0.79i$ for our
537 current aerosol composition retrievals. We estimate then the uncertainty in the
538 retrieved BC fraction using a BC refractive index of $1.75 + 0.63i$. The results of the
539 uncertainty test for retrieving BC from POLDER/PARASOL are presented in Fig. 6a.
540 As can be seen, the uncertainty strongly depends on the BC fraction and increases
541 when the BC fractions are low. We note that the uncertainty can be large (over 100
542 %) when the BC fraction is below 0.01 and aerosol loading is weak. However, the
543 uncertainty decreases rapidly and can be 50 % or better for moderate and high aerosol
544 loading (AOT at 440 nm equal or more than 0.4) and when the BC fraction is above
545 0.01. Therefore, the estimates should be quite reasonable in cases of elevated
546 pollution.
547   The reported in the literature refractive index of BrC is variable. For the forward
548 model we employed the BrC refractive index derived from Sun et al. (2007), which
549 was used to retrieve aerosol composition from ground-based remote sensing
550 measurements (e.g. Arola et al., 2011; Schuster et al., 2016). The BrC refractive
551 index, representing carbonaceous particles with light absorption in the blue and
552 ultraviolet spectral regions emitted from biomass combustion (Kirchstetter et al.,
553 2004), was used for the uncertainty estimate. The tests show (Fig. 6b) that the
554 uncertainty in BrC fraction is more than 100 % when the fractions are below 0.1 and
555 decreases to below 100 % when the BrC fractions are above 0.1 and the aerosol
556 loading is elevated. Note that the uncertainty in BrC fraction is within 50 % when the
557 fractions are above 0.1 even for very low aerosol loading (AOT = 0.05).
558   Hematite and goethite are the dominant absorbers in the coarse mode particles. The
559 hematite refractive index was selected for the employed aerosol composition mixing
560 model. The literature shows that the hematite refractive indices can also exhibit quite
561 a large range of variability (e.g. see Fig. 5b). Figure 6c thus shows the uncertainties in
562 the retrieved CAI fraction from POLDER/PARASOL associated with the hematite

Atmospheric
Chemistry
and Physics
Discussions

563 refractive given by Longtin et al. (1988) in the forward calculations and of Triaud
564 (2005) in the inversion. Except the very low fraction of CAI (below 0.005), the
565 uncertainty in CAI fraction is within 50 %.
566   The insoluble organic carbon and the non-absorbing dust present very similar
567 spectral dependence of complex refractive index (Ghosh, 1999; Koepke et al., 1997)
568 and it is practically impossible to distinguish between these species in the considered
569 in this work measurement configurations and the retrieval approach. Thus, the non-
570 absorbing insoluble organic carbon and non-absorbing mineral dust are expressed by
571 a non-absorbing insoluble species (NAI). The refractive index for the NAI in the
572 presented algorithm was taken as the dust refractive index in Ghosh (1999). The
573 uncertainty tests for the NAI fraction retrievals are presented for fine and coarse
574 fractions by replacing the dust refractive index with the refractive indices of dust
575 composed of quartz (Ghosh, 1999), kaolinite (Sokolik and Toon, 1999) and illite
576 (Sokolik and Toon, 1999) with the proportions of 48%, 26%, and 26%, respectively
577 (the proportions are recalculated from (Journet et al., 2014)) (see legend of Fig. 5).
578 The estimated uncertainties for fine and coarse NAI fractions (FNAI and CNAI)
579 decrease significantly (from 100 % to below 50 % and varying about the zero) when
580 the NAI fraction is above 0.1 (see Fig. 7a and 7b).
581   The non-absorbing insoluble can stand also for the insoluble organic carbon, as
582 was mentioned above. Thus, an additional test was conducted when the dust refractive
583 index (Ghosh, 1999) used in the forward calculations was replaced at the retrievals
584 stage by refractive index of insoluble organic carbon from Koepke et al. (1997). The
585 corresponding results of the retrieved in this case fine and coarse fractions of NAI for
586 POLDER/PARASOL observations are presented in Fig. 7c and 7d. The variability for
587 each fraction indicates that the choice of NAI refractive index can cause an
588 uncertainty in the retrieved NAI fraction less than 100% for FNAI and less than 50%
589 for CNAI when the fractions are above 0.1.
590   Figure 8 shows the uncertainties for the host species fraction (FNAS, CNAS,
591 FAWC, and CAWC), which are attributed to the differences between the refractive
592 indices and hygroscopic properties of ammonium nitrate and ammonium sulfate. The
593 uncertainties are small for FNAS, CNAS, FAWC, and CAWC, particularly when the
594 fractions are more than 0.2.
595
596

3 Application to real remote sensing data

3.1 Composition retrieval from AERONET

599   AERONET provides measurements that are among the most sensitive data to the
600 aerosol refractive index. In addition, the AOT in AERONET is result of direct
601 measurements and not retrieved as in the case of satellite observations. The GRASP
602 aerosol composition retrieval concept was therefore first tested with the real
603 AERONET data to check if the retrieved optical characteristics are consistent with the
604 results of standard AERONET product.

Atmospheric
Chemistry
and Physics
Discussions

605   Figure 9 presents the AERONET measured AOT and Ångström Exponent (870
606   nm/440 nm) and retrieved Single-Scattering Albedo (SSA) at 675 nm versus those
607   retrieved using the GRASP/Composition approach. Namely, the operational
608   AERONET product is presented versus the derived from GRASP/Composition for 3
609   sites in the African continent: Banizoumbou (data for April 2007), Skukuza (data for
610   September 2007), and Ilorin (data for January 2007), representing according to the
611   sites location and the considered seasons the dust, the biomass burning and the
612   mixture of dust and biomass burning cases, respectively. It can be seen that the
613   aerosol optical properties are reproduced very well by GRASP/Composition approach
614   not only for the recalculated AOT and its spectral behavior, but also for the SSA. The
615   mean difference in AOT is about 0.01, which is on the level of the AERONET
616   calibration uncertainty, the difference in SSA is also well within the expected retrieval
617   uncertainty of 0.03 (Dubovik et al., 2002a). There is no biases observed and the
618   correlation coefficient is nearly 1.0 for AOT and Ångström Exponent.
619   It should be mentioned here that the fine mode in the presented retrievals is
620   described by 10 bins and the coarse mode by 15 bins, which is different than the 22
621   bins that are used for the entire size distribution in the standard AERONET algorithm
622   (Fig. 9). The composition retrieval has the ability to infer different refractive indices
623   for the fine and coarse modes. This is a significant improvement over the standard
624   AERONET and POLDER/PARASOL algorithms, which allow refractive indices to
625   vary with wavelength but not with size. Indeed, the use of fixed spectral dependences
626   of the refractive indices in the GRASP/Composition algorithm provides an additional
627   constraint and reduces the number of the unknown parameters. Thus, this approach
628   makes the inversion more stable. Nevertheless, the inter-comparison of retrievals by
629   the composition approach shows full consistency with the operational AERONET
630   product, mainly thanks to an additional physical constraint on the spectral dependence
631   of refractive index.
632   In addition to the better characterization of aerosol fine and coarse modes and
633   preserving consistency in retrievals of optical characteristics, the new approach can
634   also provide insights on aerosol composition. For example, Fig. 10 shows the volume
635   fractions of aerosol species retrieved in fine and coarse modes (panels a-f), and
636   fractions of the species in the total volume (panels g-i) for the mentioned above
637   African sites. The Banizoumbou site is located near Niamey (Niger) north of the
638   Sahel, the Ilorin site (Nigeria) is located in the Sahel, and the Skukuza site is located
639   in southern Africa. The retrieved aerosol compositions for Banizoumbou and Ilorin
640   present similarity in terms of abundant dust aerosol. However, contributions of BrC
641   and BC are strong in Ilorin, and the contribution of coarse absorbing insoluble aerosol
642   fraction is strong in Banizoumbou. The southern Africa site presents a different
643   picture: a strong contribution of coarse mode soluble and of fine mode non-absorbing
644   insoluble aerosol fractions attributed to water soluble organic carbon and water
645   insoluble organic carbon in the biomass burning region, and almost twice more
646   important than in the Sahel site contribution of BC. The BrC contribution, however, is
647   about two times smaller in southern Africa than that in Sahel, which is consistent with
648   AERONET's low spectral dependence for the imaginary index. The SSA in

649 Banizoumbou is highest (0.97 at 675 nm) and in Skukuza is lowest (0.82) because
650 dust and biomass burning aerosols dominate respectively in these two regions.
651
652
653

3.2 POLDER/PARASOL satellite observations

655 After testing the aerosol composition retrieval approach with the AERONET
656 measurements, the algorithm was applied to the POLDER/PARASOL satellite
657 observations. Figures 11, 12 and Table 3 summarize an inter-comparison of aerosol
658 optical characteristics derived by the GRASP/Composition approach applied for
659 POLDER/PARASOL and those of the operational AERONET product. The inter-
660 comparison is presented for six sites in Africa and Middle East (Fig. 11) and for all
661 available AERONET data (Fig. 12) representing performance for different aerosol
662 types and on the global scale. Because of a limited sensitivity to absorption when the
663 aerosol loading is low, the SSA product is filtered for AOT at 0.440 μm equal or
664 higher than 0.4 (Dubovik et al., 2002a; Dubovik and King, 2000). The SSA and the
665 Ångström Exponent in Fig. 11 are presented for all six sites together because the
666 dynamic range of the values for each single site is limited by a dominant aerosol type.
667 It should also be noted that in the inter-comparison on the global scale (Fig. 12) the
668 correlation for Ångström Exponent was notably better for higher AOT (R of ~ 0.6 for
669 all AOTs and of ~0.8 for AOT equal or more than 0.2). The better SSA and Ångström
670 Exponent retrievals for higher AOT is, however, known also for standard retrievals
671 and other satellite products (de Leeuw et al., 2015; Popp et al., 2016). Nevertheless,
672 the good agreements for AOT (R is generally of ~ 0.9 or better), and for Ångström
673 Exponent and SSA (R of ~ 0.70 - 0.80) show that the inversion of
674 POLDER/PARASOL satellite measurements using the composition approach is
675 consistent with the ground-based AERONET reference in terms of aerosol optical
676 properties. Analysis of the per site aerosol optical properties retrievals for different
677 aerosol types (Fig. 11) also does not reveal any evident problem.
678 The selected mixing model influence on the retrievals is assessed by comparison of
679 the results from Maxwell-Garnett effective medium approximation with performance
680 using a simplified volume-weighted (VW) aerosol mixture. Definition of the species
681 constituting the VW mixing model is quite similar to Maxwell-Garnett, it employs
682 BC, BrC in fine mode, absorbing insoluble in coarse mode, non-absorbing insoluble
683 and aerosol water content in both fine and coarse modes. The tests were conducted in
684 the same manner as for the Maxwell-Garnett effective medium approximation. The
685 sensitivity tests revealed that implementation of the volume-weighted mixing rule
686 yields stable results and this model can indeed be used for the retrievals. Moreover,
687 the VW model can be preferable in some applications due to its simplicity. Figure 11
688 and Table 3 illustrate that the GRASP/Composition retrievals using the MG and VW
689 mixing models almost equally well reproduce the aerosol optical properties. The
690 inter-comparison of the standard GRASP/PARASOL retrievals (without retrieval of
691 aerosol composition) with AERONET is also presented in Fig. 11 and Table 3. It

Atmospheric
Chemistry
and Physics
Discussions

692   should noted that in all three shown cases the results obtained for AOT and Ångström
693   Exponent (AE) from PARASOL using the composition approach show comparable
694   and even better correlations with AERONET than the standard GRASP/PARASOL
695   retrieval that derives directly the spectral refractive indices instead of fractions of the
696   aerosol species with fixed refractive indices. This can be considered as confirmation
697   that the constraints adapted in the composition approach adequate provide realistic
698   and practically useful additional constraints that help to improve satellite retrievals.
699   At the same time, it can be seen that the SSA obtained by standard
700   GRASP/PARASOL correlates better with AERONET than those obtained by
701   GRASP/PARASOL composition approach. Specifically, this GRASP/PARASOL
702   composition shows systematically lower absorption than standard GRASP/PARASOL
703   retrieval. This can be explained by the fact that the complex refractive index in
704   GRASP/Composition are constrained by the information (on both magnitudes and
705   spectral tendencies) adapted from the literature while in case of standard
706   GRASP/PARASOL and operational AERONET products there are no such
707   constraints. As discussed by Dubovik and King (2000) and Dubovik et al. (2011) the
708   standard retrieval approach uses only smoothness constraints on spectral variability of
709   complex refractive index. In these regards, tests by Dubovik et al. (2000)
710   demonstrated that in presence of measurements noise the standard approach tends to
711   generate retrievals with higher values of absorption in the situation with lower aerosol
712   loading (lower AOD). This happens simply due to increased spread of SSAs for
713   situation with lower aerosol signal. Indeed, due to physical constraints SSA can not
714   higher than 1, as a result appearance of any spread caused by presence of the noise
715   generates lower SSA bias. Such bias has been often discussed by modelers
716   community as rather unfortunate feature of AERONET retrievals. Therefore, the
717   slightly higher SSA in case of GRASP/Composition can be considered rather a
718   positive effect of the additional constrain. Probably, additional focused analysis
719   should be done in future, but it can be expected that the slightly higher values in case
720   of GRASP/Composition may also on average be closer to what is expected from
721   models because tied to similar physical assumptions.

4 Illustration of global scale satellite aerosol composition retrieval

726   We processed the POLDER/PARASOL observations globally using the aerosol
727   composition retrieval algorithm. The results of this processing present the first
728   attempt to assess the measurement-based global distribution and seasonal variability
729   of aerosol composition. The data were processed for the year 2008, which provides a
730   notable variety of different aerosol types, including volcanic aerosols from a
731   Hawaiian eruption.

732   The results are further presented as seasonal means. It should be mentioned
733   however that any interpretation of the statistical values should take into account also

Atmospheric
Chemistry
and Physics
Discussions

734 the number of available observations. Therefore, it is worth presenting the global
735 maps of the number of available cloud-free pixels. Figure 13 shows that the number
736 of the cloud free pixels over land is significantly higher than over ocean, which can
737 produce a difference in the mean values and create some artificial spatial patterns. In
738 addition, the sensitivity tests and experience of remote sensing observations treatment
739 show that the accuracy of the retrievals is low and the sensitivity to absorbing aerosol
740 and refractive index variability is particularly limited when the aerosol loading is low.
741 Therefore, it is also worth presenting the global maps of the aerosol optical thickness
742 (Fig. 14), prior to analyzing the aerosol composition retrievals. It should also be
743 outlined that despite the fractions of the elements are the initial retrieval parameters,
744 direct interpretation of the maps of these fractions can be confusing because do not
745 always correspond to a significant aerosol concentration. For instance, a large fraction
746 of an element retrieved for a size mode where aerosol volume concentration is very
747 low, can have no significant meaning as not having contribution to the optical signal.
748 Therefore, the volume concentrations of the retrieved elements and not the fractions
749 will be further presented. Figures 15 to 20 thus show seasonal variabilities of the
750 retrieved aerosol volume concentrations for different aerosol species.

751

4.1 Black Carbon

753   The retrieved aerosol composition shows patterns of biomass burning in the Sahel
754 and southern Africa regions, expressed by elevated concentrations of BC (Fig. 15).
755 The derived BC concentrations show a pronounced seasonal and spatial variability.
756 The largest concentrations can be observed over the African continent, another
757 noticeable region is Asia, namely India and China. The most intensive BC emissions
758 appear during DJF, which is constituted from contributions of the Sahel region, India
759 and China. Somewhat lower concentrations during SON and JJA are attributed to
760 biomass burning regions in southern African. A global minimum of the BC
761 concentrations is during MAM. The obtained spatial and seasonal patterns of BC are
762 consistent with the knowledge that DJF is the season of intense agricultural burning
763 across the sub-Sahelian region of Africa. BC generated from such agricultural burning
764 can extend for thousands of kilometers from east to west across the continent, as can
765 be seen in Fig. 15. The BC concentration in northern Africa appears mainly over land
766 near the west coast, especially from Senegal south to Gabon on the equator, and over
767 the Gulf of Guinea, which is attributed to the biomass burning during DJF (e.g.
768 Haywood et al., 2008). The BC observed over the ocean is generally transported from
769 biomass burning areas by prevailing trade winds. The retrievals show that the BC
770 concentration in India and China, which can be rather attributed to anthropogenic
771 activity, is maximal during DJF. This result is consistent with a previous study by Li
772 et al. (2015) that also found a maximal BC mass concentration during DJF. The work
773 by Li et al. (2015) is based on retrieval of aerosol composition from AERONET
774 measurements in Beijing and Kanpur sites and presents twelve years' climatology for
775 the period 2002 - 2013.

Atmospheric
Chemistry
and Physics
Discussions

776   During JJA and SON, the elevated BC concentrations are mostly over southern
777   Africa, which is in line with the known African monsoon cycle. The variations of the
778   retrieved BC are consistent with the biomass burning activity progressing from north
779   to south Africa, starting from June, peaking in July - August and then decreasing in
780   intensity until late October with the end of the dry season (Cahoon et al., 1992;
781   Liousse et al., 1996; Maenhaut et al., 1996; Swap et al., 1996).

782   It should be reminded, however, that sensitivity to the absorption and therefore to
783   the BC signal is limited when the AOT is low. In addition, for very low AOT values
784   the aerosol volume concentrations are also low and therefore the retrieved fractions of
785   the aerosol species are more uncertain. Very low aerosol loading is typical for over
786   ocean observations (Fig. 14) and thus appearance of some BC concentrations over
787   ocean should be interpreted with caution.
788

789   **4.2 Brown Carbon**

790   Similar to BC, the observed patterns of BrC (Fig. 16) show seasonal variations,
791   primarily association with the biomass burning in Africa and the contribution of
792   Asian anthropogenic activities. A closer comparison of BrC and BC concentrations
793   reveals, however, that their maximal concentrations are not always collocated. This
794   observation reflects that fresh biomass burning aerosols have higher BC content than
795   aged aerosols (Abel et al., 2003; Haywood et al., 2003; Reid et al., 1998). During
796   SAFARI-2000, for example, the single scattering albedo has an increase from 0.84 to
797   0.90 between smoke close to the source and aged haze 5 h downwind from a large fire
798   (Abel et al., 2003), which is attributed to changes in aerosol composition. There can
799   be some rapid changes occurring in the relative concentration of particle types with
800   the aging of smoke and the BC particles become gradually more aggregated with
801   organic and sulfate particles during the aging of smoke (Pósfai et al., 2003).
802   Therefore, the more abundant presence of particles with the spectral absorption
803   signature of BC is reasonable for the areas near the biomass burning emissions,
804   whereas particles with a spectrally dependent absorption signature of BrC are
805   generally enriched in downwind region, which can explain appearance of BrC
806   concentrations in aerosol particles transported over ocean in northern hemisphere.

807

808   **4.3 Fine mode Non-Absorbing Soluble**

809   The NAS component is represented by the real part of the refractive index of
810   ammonium nitrate; however, sulfates, sea salt or aged hydroscopic particles are also
811   included in the NAS component. Figure 17 presents seasonal means of the NAS
812   retrieved for the fine mode (FNAS). The FNAS volume concentration dominates over
813   China and India, especially during DJF and SON, which can correspond to industrial
814   aerosol and heating activity in megacities with high population density. The spatial
815   patterns of FNAS also coincide with the patterns of BC in southern Africa that
816   indicates presence of non-absorbing particles fraction in the biomass burning

Atmospheric
Chemistry
and Physics
Discussions

817 emissions (e.g. water soluble organic carbon). Indeed, the carbonaceous organic
818 particles can provide a favorable surface for aging processes and sulfate nucleation
819 (Li et al., 2003). Pronounced FNAS particles concentrations are retrieved during JJA
820 over the Mediterranean Sea region, which is in line with the knowledge on abundant
821 presence of anthropogenic and biogenic sulfate particles in the Mediterranean region
822 (Ganor et al., 2000; Lelieveld et al., 2002; Levin, 2005; Levin et al., 1996). The
823 FNAS particles are also retrieved south from the Mediterranean Sea, deep inland over
824 Libya and Egypt. This FNAS component can be possible in this area considering
825 persistent north-south, north-east air mass transport in the eastern Mediterranean
826 region governed by semi-permanent low-pressure trough extending in JJA from the
827 Persian Gulf (Bitan and Sa'Aroni, 1992).
828

829 **4.4 Coarse mode Non-Absorbing Insoluble**

830 In the northern and western Africa, the coarse mode non-absorbing insoluble
831 component appears all year long with the pronounced maximum concentrations
832 during MAM to JJA (Fig. 18), representing the non-absorbing part of mineral dust.
833 Notable is a shift in the maximum of this component towards higher latitudes in JJA
834 that corresponds to the northern shift of the inter-tropical convergence zone. The
835 retrievals also clearly show a "hot spot" of coarse mode non-absorbing dust over the
836 Bodélé depression, located between the Tibesti Mountains and Lake Chad, and known
837 as the most active dust source in the Sahara desert (Gasse, 2002; Prospero et al., 2002;
838 Washington et al., 2003). This dust source is caused by the coincidence of an
839 extensive source of diatomite sediment and high velocity winds associated with the
840 Bodélé Low Level Jet (Todd et al., 2007; Washington et al., 2006; Washington and
841 Todd, 2005) with the emission peaks during DJF and MAM (Herrmann et al., 1999;
842 Koren and Kaufman, 2004; Todd et al., 2007; Washington and Todd, 2005) that are
843 also distinguishable in the presented retrievals. This CNAI aerosol type also appears
844 over the Middle East, the Arabian Peninsula and extends over Asia, which is known
845 as the global dust belt. The coarse mode non-absorbing dust concentration is
846 particularly high over the Arabian Peninsula, central to southern Pakistan, as well as
847 over the Oman and Arabian seas. Over this region, the maximum dust concentration is
848 observed during MAM and JJA, while dust concentration substantially decreases
849 during SON and DJF. Higher dust concentration during MAM and JJA is primarily
850 caused by the strong northwesterly winds known as "Shamal Wind" and dry
851 conditions. The JJA peak is caused by several major sources of dust that have
852 maximum dust activity during JJA, including desert areas in Syria and Iraq where a
853 strong northwesterly Shamal Wind is blowing (Choobari et al., 2014). The Sistan
854 region can also be distinguished among the high dust concentrations. This region is
855 considered as a major dust source in southwest Asia (Ginoux et al., 2012; Goudie,
856 2014; Léon and Legrand, 2003; Middleton, 1986a) attributed to the strong persistent
857 northeasterly winds (Alizadeh Choobari et al., 2013; Middleton, 1986b; Miri et al.,
858 2007). This source can cause frequent dust and sand storms, especially during the
859 period of June to August contributing to the deterioration of air quality (Rashki et al.,

Atmospheric
Chemistry
and Physics
Discussions

Open Access

EGU

860   2013). In addition, during DJF and SON some elevated CNAI concentrations are
861   observed in Australia (area of Lake Eyre and The Great Artesian Basin). It should be
862   also noted that some CNAI concentrations are retrieved during the seasons and over
863   the regions in Africa known for biomass burning and over south-east of USA. These
864   concentrations indicate presence of some coarse mode non-absorbing particles
865   possibly of organic origin.

866

867   **4.5 Coarse mode Absorbing Insoluble**

868   The Coarse mode Absorbing Insoluble (CAI) particles, which mainly represent the
869   iron oxides contained in mineral dust, are generally associated with the desert regions
870   and with the elevated concentrations of CNAI. The high CAI concentrations are
871   observed during MAM and JJA over western Africa and the Arabian Peninsula (Fig.
872   19). High CAI concentrations are also retrieved over Asia during the same MAM and
873   JJA seasons and are quite clearly attributed to the region of the Taklimakan desert
874   located in northwest China. It is worth noting that the maximum of CAI and CNAI do
875   not always coincide, reflecting different percentage of iron oxides in desert dust that
876   is varying depending on the soil mineralogy of the source region. Calculations of the
877   ratio of CAI to CNAI concentrations over African continent provided values of up to
878   about 0.05, which is consistent with up to 3 to 5 % iron oxides in desert dust (e.g.
879   Ganor and Foner, 1996; Guieu et al., 2002; Zhang et al., 2003; Lafon et al., 2004).

880   The high CAI concentrations over western Africa are mainly present over Niger,
881   Mauritania and near the west coast. This is in line with a study by Formenti et al.
882   (2008) that demonstrates the higher iron oxide content in Sahelian dust originated
883   from the Sahel belt, while a lower content is in the Chad basin. Lázaro et al. (2008)
884   also reported that the iron oxide content of dust transported to the Canary Islands,
885   near the west coast, tends to have higher values for source areas between 0°N - 20°N.
886   In addition, high CAI concentrations are also derived over the Arabian Peninsula and
887   the Arabian Sea, which may be attributed to the dust originated from Saudi Arabia,
888   known for presence of an important iron content (Krueger et al., 2004). It should be
889   mentioned here that a discontinuity in the retrieved concentrations can be noted
890   between over land and over water in the regions of the Red Sea and Arabian Sea.
891   Given that such discontinuity does not appear in all coastal regions, but only in
892   particular circumstances, we suppose that there are some physical explanations. For
893   instance, the observed discontinuity corresponds well to the land topography, i.e.
894   presence of surrounding mountains and the observed in other work accumulation of
895   aerosol over the Red Sea (Brindley et al., 2015). It is also interesting to admit that
896   some coarse mode absorbing aerosol appear in the regions and seasons associated
897   with biomass burning and elevated concentrations of BrC and BC in the fine mode,
898   e.g. in Africa during DJF and SON seasons. This fact can reflect presence of
899   absorbing carbonaceous material in the coarse mode, which was fitted by refractive
900   index of iron oxide assumed as only the absorbing component of the coarse mode.

Atmospheric
Chemistry
and Physics
Discussions

901
4.6 Fine mode Non-Absorbing Insoluble

903   Because the fine mode non-absorbing insoluble component (Fig. 20) can stand for
904 both OC and non-absorbing dust, the Ångström Exponent can be used as an additional
905 post retrieval criteria for a better interpretation of this component. For instance, the
906 joint FNAI and Ångström Exponent (maps are presented in supplementary material)
907 analysis shows that the particles concentrations derived over western Africa, Middle
908 East, Central Asia and northwest China mainly reflect presence of fine mode non-
909 absorbing dust because are associated with the values of Ångström Exponent
910 generally well below one. Specific examples are the concentrations derived over the
911 Bodélé depression during DJF, the Taklimakan desert in China during MAM and
912 Arabian Peninsula during JJA. However, the elevated FNAI particles concentrations
913 retrieved over southern Africa and South America during JJA and SON, over eastern
914 part of China and Siberia during JJA, and generally over India, are associated with
915 high values of Ångström Exponent, thus should rather be classified as organic carbon.
916 For example, high OC in southern China (Sichuan Basin and the Pearl River Delta
917 region) and urban south Asia is confirmed in several previous studies (Decesari et al.,
918 2010; Stone et al., 2010; Zhang et al., 2008b; Zhang et al., 2012). The OC of urban
919 origin in China is enhanced around May to June and October (Zhang et al., 2012),
920 which may be an explanation of the retrieved high OC concentration during JJA in
921 southern China. Secondary OC (SOC) can also contribute to the total concentrations
922 of OC (Miyazaki et al., 2006; Weber et al., 2007; Zhang et al., 2008b; Zhang et al.,
923 2005) and be retrieved here as FNAI. Additionally, the elevated OC concentration
924 over South America during SON correspond well to the known season of biomass
925 burning that starts in July and peaks generally in August and September (Duncan et
926 al., 2003).

927   A plume structure of elevated fine non-absorbing insoluble (Fig. 20) and soluble
928 (Fig. 17) components originated from Hawaiian Islands in the North Pacific Ocean is
929 also notable. This structure is visible during three seasons from MAM to SON and
930 corresponds to a Hawaiian volcano emission. The material emitted into the
931 atmosphere in this case was not the coarse volcanic ash, but continuous gaseous
932 emissions that can form secondary aerosol during downwind transport (Craddock and
933 Greeley, 2009; Edmonds et al., 2013). Identification of this material by the suggested
934 approach as a mixture of components equivalent to ammonium sulfate and fine non-
935 absorbing dust is therefore quite plausible.

936
4.7 Aerosol Water Content and Coarse mode Non-Absorbing Soluble

938   The algorithm also provides aerosol water content that is required to create the host
939 by mixture with non-absorbing soluble component. As result, the retrieved spatial and
940 temporal patterns of aerosol water content and non-absorbing soluble are very similar.
941 That is, the fine mode aerosol water content is mainly retrieved in the regions with

Atmospheric
Chemistry
and Physics
Discussions
Open Access
EGU

942 high loading of anthropogenic aerosol, similarly to the fine mode non-absorbing
943 soluble. For instance, the fine mode aerosol water content can be seen over India and
944 China during SON and DJF, at high latitudes of northern hemisphere and over Eurasia
945 during SON. Some notable water concentrations are also retrieved over southern
946 Africa during the biomass burning season (JJA), but mainly over ocean that
947 correspond to visibly transported and likely aged aerosol. The maps of FAWC are
948 presented in the supplementary material as they are very similar to already presented
949 FNAS (Fig. 17).

950 The retrieved coarse mode aerosol water content and coarse non-absorbing
951 soluble also present very similar spatial and temporal patterns. However, they are
952 different from the patterns of fine mode. The concentrations are very low everywhere,
953 except over ocean in the regions associated with high concentrations of the coarse
954 non-absorbing insoluble (dust) component. This feature is associated with dust
955 transported from western Africa and Arabian Peninsula. These coarse mode AWC
956 and NAS retrievals require a careful interpretation. First, it should be realized that
957 even relatively small aerosol water fraction retrieved in the regions of very high
958 aerosol concentration can result in a pronounced volume concentration. In addition,
959 aerosols with low real refractive index, which cannot be fully explained by the
960 assumed dust aerosol model, will be interpreted as a water fraction. For instance,
961 some low water aerosol concentration erroneously appears over the Bodélé depression
962 during DJF. The Bodélé dust, however, is known to contain much fossil diatom
963 (Formenti et al., 2008), which would have a different real part of refractive index then
964 assumed in this study mixture of quartz, kaolinite and illite. At the same time,
965 possible hygroscopicity of mineral dust, its coating by organics and internal mixture
966 with sea salt, were found in several laboratory and field studies (e.g. Usher et al.,
967 2003; Falkovich et al., 2004; Laskin et al., 2005; Derimian et al., 2017). The fact that
968 the notable aerosol water content is observed in the retrievals only over ocean and not
969 over land, except for retrievals over Bodélé, also agrees with hypothesis of the dust
970 hygroscopicity. We therefore conclude that despite this pronounced water aerosol
971 content in the coarse mode should be questioned and interpreted with caution, a
972 physical significance of this result should not be excluded. Indeed, this retrieval result
973 may not be fully understood at present but it was not enforced by any specific
974 assumption or measurement artifact, and therefore it is likely to represent a
975 manifestation of specific physical or chemical transformation of aerosol or properties
976 of dust. In addition to the described above main feature of CAWC and CNAS, the
977 derived maps are presented in supplements, together with the maps of FAWC, which
978 are similar to already presented FNAS.

979

5 Conclusions

981 We present a new approach for monitoring atmospheric aerosol composition with
982 remote sensing observations. Unlike existing aerosol composition retrieval algorithms
983 that interpret an intermediate retrieval of the refractive index, this study utilizes a

Atmospheric
Chemistry
and Physics
Discussions

984   direct fit of measurements. We demonstrate retrievals of several aerosol components
985   in fine and coarse size modes under assumption of an internal aerosol mixing rule.
986   The tests using a volume weighted mixing rule were also conducted and the results
987   compared.

988   The approach is implemented in a state of the art GRASP algorithm (Dubovik et
989   al., 2014, 2011) designed to process space-borne and ground-based remote sensing
990   observations. The composition module is incorporated in GRASP thus the new
991   GRASP/Composition version of the code employs mixtures of aerosol components
992   with known refractive indices. This approach serves also as an additional physical
993   constraint on spectral dependences of complex refractive index. The composition
994   module uses the Maxwell-Garnett effective medium approximation (EMA) and is
995   based on the Schuster et al. (2016, 2009) approach, but assumes independent aerosol
996   mixtures in the fine and coarse modes and the direct fit of radiances instead of an
997   intermedia step of fitting the retrieved refractive indices.

998   A series of numerical sensitivity tests with synthetic data were conducted to
999   evaluate the composition retrieval. Results of the tests showed that the new
1000   conversion module allows the retrieval to distinguish amongst several assumed
1001   aerosol components. The tests with the new module also show consistency with
1002   GRASP tests that are traditionally configured for ground-based AERONET
1003   measurements.

1004   We also tested the algorithm with real measurements. Application of the
1005   GRASP/Composition algorithm to the AERONET Sun/sky photometric
1006   measurements retrievals of AOT, Ångström Exponent and SSA presented good
1007   agreement with the standard operational AERONET product for sites dominated by
1008   dust, biomass burning, and mixtures of dust and biomass burning aerosol. In addition,
1009   because of the reduced number of parameters (instead of 8 parameters for complex
1010   refractive index retrievals using 6 parameters for composition retrievals) and an
1011   additional physical constrain on spectral dependence of refractive index in the
1012   composition retrieval, the GRASP/Composition approach applied for AERONET can
1013   split the characteristics of fine and coarse mode aerosol. The GRASP/Composition
1014   algorithm was also applied for the POLDER/PARASOL satellite observations. An
1015   inter-comparison of aerosol optical characteristics derived from POLDER/PARASOL
1016   using the composition approach and those of the AERONET operational product
1017   demonstrated a high reliability of the results.

1018   The performance of the aerosol composition algorithm has been demonstrated by
1019   the application to POLDER/PARASOL observations on the global scale for year
1020   2008. The obtained spatial and temporal patterns of aerosol composition distribution
1021   seem to agree well with known physical expectations. For a proper interpretation of
1022   the obtained results it should be also realized that the retrieved aerosol species and
1023   their concentrations compose a set of parameters that reproduces well the measured
1024   radiation field and provides adequate retrieved optical properties of aerosol. At the
1025   same time, the direct interpretation from the chemical point of view is not always

Atmospheric
Chemistry
and Physics
Discussions

1026   evident and even possible. For instance, as mentioned in the methodology part, the
1027   distinguishing of some chemical species is not possible for the given configuration of
1028   remote sensing measurements. However, the retrieved composition still reflects the
1029   aerosol microphysics and chemistry, and their variability. One should also remember
1030   that, based on the sensitivity tests and experience of aerosol characterization by
1031   remote sensing, the accuracy of the retrievals depends on the aerosol loading (AOT).
1032   Accuracy of the absorbing components retrieval can be primary affected. Thus,
1033   interpretation of all the obtained patters requires a more detailed analysis and it is
1034   realized that some erroneous composition features can be possible. The principle
1035   limitations of the presented approach are: (i) lack of sensitivity to absorption species
1036   in case of low AOT; (ii) difficulty to distinguish between iron oxide and absorbing
1037   carbonaceous species (BrC and BC), which is mainly related to the limited number of
1038   spectral channels in shortwave solar spectrum; (iii) non-absorbing insoluble
1039   component can include organic material, but also non-absorbing dust. These
1040   assumptions can lead to some misinterpretation; for instance, the analysis of the BrC
1041   retrievals at some locations reveals that the aerosol absorbing properties attributed to
1042   BrC should be attributed to the iron oxides that are present in the fine size fraction. A
1043   post-retrieval classification is helpful to resolve the shortcomings. For example,
1044   analysis of Ångström Exponent can indicate dominance of coarse particles of mineral
1045   dust origin or fine particles of combustion origin, which can provide more
1046   information about the non-absorbing insoluble component.

1047   Nevertheless, the results are encouraging. For example, the derived BC and BrC
1048   exhibit a seasonal and spatial variability that is attributed to the known biomass
1049   burning season cycle in Africa and the anthropogenic pollution patterns in Asia, in
1050   particular India and China. Coarse mode absorbing (mainly iron oxides) and non-
1051   absorbing (mainly dust) insoluble components show a similar seasonal and spatial
1052   variability, reaching a peak during MAM and a minimum during SON. It is also noted
1053   that the maximums of iron oxide concentration are not co-located with those of dust,
1054   because the elemental and mineralogical compositions of mineral dust vary depending
1055   on the source region. The global dust belt extending from western Africa, through the
1056   Middle East to Central Asia is also observed in the composition retrieval.
1057   GRASP/Composition indicates high concentrations of non-absorbing insoluble appear
1058   over the Sahara, Arabian Peninsula, Caspian Sea and Aral Sea regions in Central
1059   Asia, and the Gobi and Taklimakan desert in China. In addition, dust was also
1060   detected over some regions in Australia during DJF and SON.

1061   The composition retrieval algorithm demonstrated here using AERONET and
1062   POLDER/PARASOL data can also be used for interpreting other observations. That
1063   is, the composition approach is now incorporated in the GRASP algorithm, which has
1064   a generalized input and can be easily modified and adapted to other both passive and
1065   active remote sensing instruments, for example, the Directional Polarimetric Camera
1066   (DPC) launched onboard the GaoFen-5 Satellite in Chinese High-resolution Earth
1067   Observation Program, which is the first Chinese multi-angle polarized earth
1068   observation satellite sensor (Dubovik et al., 2019; Li et al., 2018). Moreover, the

Atmospheric
Chemistry
and Physics
Discussions

1069 proposed aerosol parameterization using components can be helpful not only for
1070 retrieving additional information about aerosol composition, but also for optimizing
1071 retrieval stability.

1072 Additionally, we tested the volume-weighted mixing model, in addition to the
1073 Maxwell-Garnett EMA, to evaluate the sensitivity of our approach to the assumed
1074 aerosol EMA. We tested both approaches using our suite of aerosol species (i.e. BC,
1075 BrC, coarse mode absorbing insoluble, fine and coarse mode non-absorbing
1076 insoluble). The sensitivity tests revealed that implementation of the volume-weighted
1077 mixing rule also presents stable results that are consistent with the Maxwell-Garnett
1078 EMA. Thus, the volume-weighted model can also be employed in
1079 GRASP/composition retrieval, and may be preferable in some applications due to its
1080 simplicity.

1081 The results of the aerosol composition retrieval from AERONET and
1082 POLDER/PARASOL satellite measurements demonstrate a potential for constraining
1083 global and regional aerosol modeling that can be particularly valuable because no
1084 other aerosol composition data are often available on a large spatial and temporal
1085 scale.

1086

1089

1090 **Author contributions:** LL, OD, YD and GLS contributed to retrieval algorithm
1091 development and conducted the sensitivity and uncertainty tests using synthetic data.
1092 TL, PL, FD, DF and CC contributed to the modifications of GRASP code. ZL, AL,
1093 BT and HC contributed to the retrievals derived from AERONET measurements. LL,
1094 OD and YD wrote the paper with input from all authors.

1095

1096 **Competing interests**: The authors declare that they have no conflict of interest.

1097

Atmospheric
Chemistry
and Physics
Discussions

1109
Reference:
1111

1112 Abel, S.J., Haywood, J.M., Highwood, E.J., Li, J., Buseck, P.R.: Evolution of biomass
1113   burning aerosol properties from an agricultural fire in southern Africa, Geophys. Res.
1114   Lett., 30, 10–13, https://doi.org/10.1029/2003GL017342, 2003.
1115 Alizadeh Choobari, O., Zawar-Reza, P., Sturman, A.: Low level jet intensification by mineral
1116   dust aerosols, Ann. Geophys., 31, 625–632, https://doi.org/10.5194/angeo-31-625-2013,
1117   2013.
1118 Andreae, M.O. and Gelencsér, A.: Black carbon or brown carbon? the nature of light-
1119   absorbing carbonaceous aerosols, Atmos. Chem. Phys., 6, 3131–3148,
1120   https://doi.org/10.5194/acp-6-3131-2006, 2006.
1121 Arimoto, R., Balsam, W., Schloesslin, C.: Visible spectroscopy of aerosol particles collected
1122   on filters: Iron-oxide minerals, Atmos. Environ., 36, 89–96,
1123   https://doi.org/10.1016/S1352-2310(01)00465-4, 2002.
1124 Arola, A., Schuster, G., Myhre, G., Kazadzis, S., Dey, S., Tripathi, S.N.: Inferring absorbing
1125   organic carbon content from AERONET data, Atmos. Chem. Phys., 11, 215–225,
1126   https://doi.org/10.5194/acp-11-215-2011, 2011.
1127 Benavent-oltra, J.A., Román, R., Granados-muñoz, M.J., Pérez-ramírez, D.: Comparative
1128   assessment of GRASP algorithm for a dust event over Granada (Spain) during
1129   ChArMEx-ADRIMED 2013 campaign, Atmos. Meas. Tech., 10, 4439–4457,
1130   https://doi.org/10.5194/amt-10-4439-2017, 2017.
1131 Bitan, A. and Sa'Aroni, H.: The horizontal and vertical extension of the Persian Gulf pressure
1132   trough, Int. J. Climatol., 12, 733–747, https://doi.org/10.1002/joc.3370120706, 1992.
1133 Bohren, C.F. and Huffman, D.R.: Scattering Coefficients, in: Absorption and Scattering of
1134   Light by Small Particles, 1983.
1135 Bond, T.C. and Bergstrom, R.W.: Light Absorption by Carbonaceous Particles: An
1136   Investigative Review, Aerosol Sci. Technol., 40, 27–67,
1137   https://doi.org/10.1080/02786820500421521, 2006.
1138 Bond, T.C., Charlson, R.J., Heintzenberg, J.: Quantifying the emission of light-absorbing
1139   particles: Measurements tailored to climate studies, Geophys. Res. Lett., 25, 337–340,
1140   https://doi.org/10.1029/98GL00039, 1998.
1141 Bond, T.C., Doherty, S.J., Fahey, D.W., Forster, P.M., Berntsen, T., Deangelo, B.J., Flanner,
1142   M.G., Ghan, S., Kärcher, B., Koch, D., Kinne, S., Kondo, Y., Quinn, P.K., Sarofim,
1143   M.C., Schultz, M.G., Schulz, M., Venkataraman, C., Zhang, H., Zhang, S., Bellouin, N.,
1144   Guttikunda, S.K., Hopke, P.K., Jacobson, M.Z., Kaiser, J.W., Klimont, Z., Lohmann,
1145   U., Schwarz, J.P., Shindell, D., Storelvmo, T., Warren, S.G., Zender, C.S.: Bounding the
1146   role of black carbon in the climate system: A scientific assessment, J. Geophys. Res.
1147   Atmos., 118, 5380–5552, https://doi.org/10.1002/jgrd.50171, 2013.
1148 Brindley, H., Osipov, S., Bantges, R., Smirnov, A., Banks, J., Levy, R., Jish Prakash, P.,
1149   Stenchikov, G.: An assessment of the quality of aerosol retrievals over the Red Sea and
1150   evaluation of the climatological cloud-free dust direct radiative effect in the region, J.
1151   Geophys. Res. Atmos., 120, 10862-10878, https://doi.org/10.1002/2015JD023282,
1152   2015.
1153 Cahoon, D.R., Stocks, B.J., Levine, J.S., Cofer, W.R., O'Neill, K.P.: Seasonal distribution of
1154   African savanna fires, Nature, 359, 812–815, https://doi.org/10.1038/359812a0, 1992.
1155 Chakrabarty, R.K., Moosmüller, H., Chen, L.W.A., Lewis, K., Arnott, W.P., Mazzoleni, C.,
1156   Dubey, M.K., Wold, C.E., Hao, W.M., Kreidenweis, S.M.: Brown carbon in tar balls
1157   from smoldering biomass combustion, Atmos. Chem. Phys., 10, 6363–6370,
1158   https://doi.org/10.5194/acp-10-6363-2010, 2010.
1159 Chami, M., Santer, R., Dilligeard, E. : Radiative transfer model for the computation of
1160   radiance and polarization in an ocean–atmosphere system: polarization properties of
1161   suspended matter for remote sensing, Appl. Opt., 40, 2398,
1162   https://doi.org/10.1038/laban1011-313, 2001.

Chen, C., Dubovik, O., Henze, D.K., Lapyonak, T., Chin, M., Ducos, F., Litvinov, P., Huang, X., Li, L.: Retrieval of desert dust and carbonaceous aerosol emissions over Africa from POLDER/PARASOL products generated by the GRASP algorithm, Atmos. Chem. Phys., 18, 12551–12580, https://doi.org/10.5194/acp-18-12551-2018, 2018.

Chen, C.T. and Cahan, B.D.: Visible and ultraviolet optical properties of single-crystal and polycrystalline hematite measured by spectroscopic ellipsometry, J. Opt. Soc. Am., 71, 932–934, 1981.

Chen, Y. and Bond, T.C.: Light absorption by organic carbon from wood combustion, Atmos. Chem. Phys., 10, 1773–1787, 2010.

Choobari, O.A., Zawar-Reza, P., Sturman, A.: The global distribution of mineral dust and its impacts on the climate system: A review, Atmos. Res., 138, 152–165, https://doi.org/10.1016/j.atmosres.2013.11.007, 2014.

Chowdhary, J., Cairns, B., Travis, L.D.: Contribution of water-leaving radiances to multiangle, multispectral polarimetric observations over the open ocean: bio-optical model results for case 1 waters, Appl. Opt., 45, 5542–67, https://doi.org/10.1364/AO.45.005542, 2006.

Collins, W.D., Rasch, P.J., Eaton, B.E., Khattatov, B. V, Lamarque, J.-F., Zender, C.S.: Simulating aerosols using a chemical transport model with assimilation of satellite aerosol retrievals: Methodology for INDOEX, J. Geophys. Res. Atmos., 106, 7313–7336, https://doi.org/10.1029/2000JD900507, 2001.

Cooke, W.F., Liousse, C., Cachier, H., Feichter, J.: Construction of a 1° × 1° fossil fuel emission data set for carbonaceous aerosol and implementation and radiative impact in the ECHAM4 model, J. Geophys. Res. Atmos., 104, 22137–22162, https://doi.org/10.1029/1999JD900187, 1999.

Cox, C. and Munk, W.: Measurement of the Roughness of the Sea Surface from Photographs of the Sun's Glitter, J. Opt. Soc. Am., 44, 838, https://doi.org/10.1364/JOSA.44.000838, 1954.

Craddock, R.A. and Greeley, R.: Minimum estimates of the amount and timing of gases released into the martian atmosphere from volcanic eruptions, Icarus, 204, 512–526, https://doi.org/10.1016/j.icarus.2009.07.026, 2009.

de Leeuw, G., Holzer-Popp, T., Bevan, S., Davies, W.H., Descloitres, J., Grainger, R.G., Griesfeller, J., Heckel, A., Kinne, S., Klüser, L., Kolmonen, P., Litvinov, P., Martynenko, D., North, P., Ovigneur, B., Pascal, N., Poulsen, C., Ramon, D., Schulz, M., Siddans, R., Sogacheva, L., Tanré, D., Thomas, G.E., Virtanen, T.H., von Hoyningen Huene, W., Vountas, M., Pinnock, S.: Evaluation of seven European aerosol optical depth retrieval algorithms for climate analysis, Remote Sens. Environ., 162, 295–315, https://doi.org/10.1016/j.rse.2013.04.023, 2015.

Decesari, S., Facchini, M.C., Carbone, C., Giulianelli, L., Rinaldi, M., Finessi, E., Fuzzi, S., Marinoni, A., Cristofanelli, P., Duchi, R., Bonasoni, P., Vuillermoz, E., Cozic, J., Jaffrezo, J.L., Laj, P.: Chemical composition of PM10 and PM1 at the high-altitude Himalayan station Nepal Climate Observatory-Pyramid (NCO-P) (5079 m a.s.l.), Atmos. Chem. Phys., 10, 4583–4596, https://doi.org/10.5194/acp-10-4583-2010, 2010.

Derimian, Y., Choel, M., Rudich, Y., Deboudt, K., Dubovik, O., Laskin, A., Legrand, M., Damiri, B., Koren, I., Unga, F., Moreau, M., Andreae, M. O., Karnieli, A.: Effect of sea breeze circulation on aerosol mixing state and radiative properties in a desert setting, Atmos. Chem. Phys., 17, 11331-11353, https://doi.org/10.5194/acp-17-11331-2017, 2017.

Derimian, Y., Karnieli, A., Kaufman, Y.J., Andreae, M.O., Andreae, T.W., Dubovik, O., Maenhaut, W., Koren, I.: The role of iron and black carbon in aerosol light absorption, Atmos. Chem. Phys., 8, 3632–3637, 2008.

Deschamps, P.Y., Buriez, J.C., Bréon, F.M., Leroy, M., Podaire, A., Bricaud, A., Sèze, G.: The POLDER Mission: Instrument Characteristics and Scientific Objectives, IEEE Trans. Geosci. Remote Sens., 32, 598–615, https://doi.org/10.1109/36.297978, 1994.

Deuzé, J.L., Bréon, F.M., Devaux, C., Goloub, P., Herman, M., Lafrance, B., Maignan, F., Marchand, A., Nadal, F., Perry, G., Tanré, D.: Remote sensing of aerosols over land

surfaces from POLDER-ADEOS-1 polarized measurements, J. Geophys. Res. Atmos., 106, 4913–4926, https://doi.org/10.1029/2000JD900364, 2001.

Dinar, E., Abo Riziq, A., Spindler, C., Erlick, C., Kiss, G., Rudich, Y., The complex refractive index of atmospheric and model humic-like substances (HULIS) retrieved by a cavity ring down aerosol spectrometer (CRD-AS), Faraday Discuss., 137, 279–295, https://doi.org/10.1039/b703111d, 2007.

Downing, H.D. and Williams, D.: Optical constants of water in the infrared, J. Geophys. Res., 80, 1656–1661, https://doi.org/10.1029/JC080i012p01656, 1975.

Dubovik, O.: Optimization of Numerical Inversion in Photopolarimetric Remote Sensing, in: Photopolarimetry in Remote Sensing, Kluwer Academic Publishers, Dordrecht, pp. 65–106, https://doi.org/10.1007/1-4020-2368-5_3, 2004.

Dubovik, O., Herman, M., Holdak, A., Lapyonok, T., Tanré, D., Deuzé, J.L., Ducos, F., Sinyuk, A., Lopatin, A.: Statistically optimized inversion algorithm for enhanced retrieval of aerosol properties from spectral multi-angle polarimetric satellite observations, Atmos. Meas. Tech., 4, 975–1018, https://doi.org/10.5194/amt-4-975-2011, 2011.

Dubovik, O., Holben, B., Eck, T.F., Smirnov, A., Kaufman, Y.J., King, M.D., Tanré, D., Slutsker, I.: Variability of Absorption and Optical Properties of Key Aerosol Types Observed in Worldwide Locations, J. Atmos. Sci., 59, 590–608, 2002a.

Dubovik, O., Holben, B.N., Lapyonok, T., Sinyuk, A., Mishchenko, M.I., Yang, P., Slutsker, I.: Non-spherical aerosol retrieval method employing light scattering by spheroids, Geophys. Res. Lett., 29, 541-544, https://doi.org/10.1029/2001GL014506, 2002b.

Dubovik, O. and King, M.D.: A flexible inversion algorithm for retrieval of aerosol optical properties from Sun and sky radiance measurements, J. Geophys. Res. Atmos., 105, 20673–20696, https://doi.org/10.1029/2000JD900282, 2000.

Dubovik, O., Lapyonok, T., Kaufman, Y.J., Chin, M., Ginoux, P., Kahn, R. a., Sinyuk, a.: Retrieving global aerosol sources from satellites using inverse modeling, Atmos. Chem. Phys., 8, 209–250, https://doi.org/10.5194/acp-8-209-2008, 2008.

Dubovik, O., Lapyonok, T., Litvinov, P., Herman, M., Fuertes, D., Ducos, F., Torres, B., Derimian, Y., Huang, X., Lopatin, A., Chaikovsky, A., Aspetsberger, M., Federspiel, C.: GRASP: a versatile algorithm for characterizing the atmosphere, SPIE Newsroom 2–5, https://doi.org/10.1117/2.1201408.005558, 2014.

Dubovik, O., Li, Z., Mishchenko, M.I., Tanré, D., Karol, Y., Bojkov, B., Cairns, B., Diner, D.J., Espinosa, W.R., Goloub, P., Gu, X., Hasekamp, O., Hong, J., Hou, W., Knobelspiesse, K.D., Landgraf, J., Li, L., Litvinov, P., Liu, Y., Lopatin, A., Marbach, T., Maring, H., Martins, V., Meijer, Y., Milinevsky, G., Mukai, S., Parol, F., Qiao, Y., Remer, L., Rietjens, J., Sano, I., Stammes, P., Stamnes, S., Sun, X., Tabary, P., Travis, L.D., Waquet, F., Xu, F., Yan, C., Yin, D.: Polarimetric remote sensing of atmospheric aerosols: Instruments, methodologies, results, and perspectives, J. Quant. Spectrosc. Radiat. Transf., 224, 474–511, https://doi.org/10.1016/j.jqsrt.2018.11.024, 2019.

Dubovik, O., Sinyuk, A., Lapyonok, T., Holben, B.N., Mishchenko, M., Yang, P., Eck, T.F., Volten, H., Muñoz, O., Veihelmann, B., van der Zande, W.J., Leon, J.F., Sorokin, M., Slutsker, I.: Application of spheroid models to account for aerosol particle nonsphericity in remote sensing of desert dust, J. Geophys. Res. Atmos., 111, 1–34, https://doi.org/10.1029/2005JD006619, 2006.

Duncan, B.N., Martin, R. V., Staudt, A.C., Yevich, R., Logan, J.A.: Interannual and seasonal variability of biomass burning emissions constrained by satellite observations, J. Geophys. Res., 108, 4100, https://doi.org/10.1029/2002JD002378, 2003.

Edmonds, M., Sides, I.R., Swanson, D.A., Werner, C., Martin, R.S., Mather, T.A., Herd, R.A., Jones, R.L., Mead, M.I., Sawyer, G., Roberts, T.J., Sutton, A.J., Elias, T.: Magma storage, transport and degassing during the 2008-10 summit eruption at Kilauea Volcano, Hawaii, Geochim. Cosmochim. Acta., 123, 284–301, https://doi.org/10.1016/j.gca.2013.05.038, 2013.

Espinosa, W.R., Remer, L.A., Dubovik, O., Ziemba, L., Beyersdorf, A., Orozco, D., Schuster, G., Lapyonok, T., Fuertes, D., Martins, J.V.: Retrievals of aerosol optical and

Atmospheric
Chemistry
and Physics
Discussions

1273   microphysical properties from Imaging Polar Nephelometer scattering measurements,
1274   Atmos. Meas. Tech., 10, 811–824, https://doi.org/10.5194/amt-10-811-2017, 2017.
1275 Falkovich, A. H., Schkolnik, G., Ganor, E., Rudich, Y.: Adsorption of organic compounds
1276   pertinent to urban environments onto mineral dust particles, J. Geophys. Res. Atmos.,
1277   109, https://doi.org/10.1029/2003jd003919, 2004.
1278 Formenti, P., Caquineau, S., Chevaillier, S., Klaver, A., Desboeufs, K., Rajot, J.L., Belin, S.,
1279   Briois, V.: Dominance of goethite over hematite in iron oxides of mineral dust from
1280   Western Africa: Quantitative partitioning by X-ray absorption spectroscopy, J. Geophys.
1281   Res. Atmos., 119, 12740-12754, https://doi.org/10.1002/2014JD021668, 2014.
1282 Formenti, P., Rajot, J.L., Desboeufs, K., Caquineau, S., Chevaillier, S., Nava, S., Gaudichet,
1283   A., Journet, E., Triquet, S., Alfaro, S., Chiari, M., Haywood, J., Coe, H., Highwood, E.:
1284   Regional variability of the composition of mineral dust from western Africa: Results
1285   from the AMMA SOP0/DABEX and DODO field campaigns, J. Geophys. Res. Atmos.,
1286   113, 1–12, https://doi.org/10.1029/2008JD009903, 2008.
1287 Ganor, E. and Foner, H. A.: The mineralogical and chemical properties and the behavior of
1288   aeolian Saharan dust over Israel, in: The Impact of Desert Dust Across the
1289   Mediterranean, edited by: Guerzoni, S., and Chester, R., Kluwer Academic Publishers,
1290   Printed in the Netherlands, 163-172, 1996.
1291 Ganor, E., Foner, H.A., Bingemer, H.G., Udisti, R., Setter, I.: Biogenic sulphate generation in
1292   the Mediterranean Sea and its contribution to the sulphate anomaly in the aerosol over
1293   Israel and the Eastern Mediterranean, Atmos. Environ., 34, 3453–3462,
1294   https://doi.org/10.1016/S1352-2310(00)00077-7, 2000.
1295 Gasse, F.: Diatom-inferred salinity and carbonate oxygen isotopes in Holocene waterbodies
1296   of the western Sahara and Sahel (Africa), Quat. Sci. Rev., 21, 737–767,
1297   https://doi.org/10.1016/S0277-3791(01)00125-1, 2002.
1298 Ghosh, G.: Dispersion-equation coefficients for the refractive index and birefringence of
1299   calcite and quartz crystals, Opt. Commun., 163, 95–102, https://doi.org/10.1016/S0030-
1300   4018(99)00091-7, 1999.
1301 Ginoux, P., Prospero, J.M., Gill, T.E., Hsu, N.C., Zhao, M.: Global-scale attribution of
1302   anthropogenic and natural dust sources and their emission rates based on MODIS Deep
1303   Blue aerosol products, Rev. Geophys., 50, 1–36,
1304   https://doi.org/10.1029/2012RG000388, 2012.
1305 Gosse, S.F., Wang, M., Labrie, D., Chylek, P.: Imaginary part of the refractive index of
1306   sulfates and nitrates in the 0.7-2.6-micron spectral region, Appl. Opt., 36, 3622–3634,
1307   1997.
1308 Goudie, A.S.: Desert dust and human health disorders, Environ. Int., 63, 101–113,
1309   https://doi.org/10.1016/j.envint.2013.10.011, 2014.
1310 Guieu, C., Loye-Pilot, M. D., Ridame, C., Thomas, C.: Chemical characterization of the
1311   Saharan dust end-member: Some biogeochemical implications for the western
1312   Mediterranean Sea, J. Geophys. Res., 107 (D15), 4258,
1313   https://doi.org/4210.1029/2001JD000582, 2002.
1314 Hale, G.M. and Querry, M.R.: Optical Constants of Water in the 200-nm to 200-microm
1315   Wavelength Region, Appl. Opt., 12, 555–563, https://doi.org/10.1364/AO.12.000555,
1316   1973.
1317 Haywood, J.M., Osborne, S.R., Francis, P.N., Keil, A., Formenti, P., Andreae, M.O., Kaye,
1318   P.H.: The mean physical and optical properties of regional haze dominated by biomass
1319   burning aerosol measured from the C-130 aircraft during SAFARI 2000, J. Geophys.
1320   Res. Atmos., 108, 1–9, https://doi.org/10.1029/2002JD002226, 2003.
1321 Haywood, J. M., Pelon, J., Formenti, P., Bharmal, N., Brooks, M., Capes, G., Chazette, P.,
1322   Chou, C., Christopher, S., Coe, H., Cuesta, J., Derimian, Y., Desboeufs, K., Greed, G.,
1323   Harrison, M., Heese, B., Highwood, E. J., Johnson, B., Mallet, M., Marticorena, B.,
1324   Marsham, J., Milton, S., Myhre, G., Osborne, S. R., Parker, D. J., Rajot, J. L., Schulz,
1325   M., Slingo, A., Tanre, D., Tulet, P.: Overview of the Dust and Biomass-burning
1326   Experiment and African Monsoon Multidisciplinary Analysis Special Observing Period-
1327   0, J. Geophys. Res. Atmos., 113, https://doi.org/10.1029/2008jd010077, 2008.

Haywood, J.M. and Shine, K.P.: The effect of anthropogenic sulfate and soot aerosol on the clear sky planetary radiation budget, Geophys. Res. Lett., 22, 603–606, https://doi.org/10.1029/95GL00075, 1995.

Henze, D.K., Hakami, A., Seinfeld, J.H.: Development of the adjoint of GEOS-Chem, Atmos. Chem. Phys., 7, 2413–2433, https://doi.org/10.5194/acp-7-2413-2007, 2007.

Herman, M., Deuzé, J.L., Marchand, A., Roger, B., Lallart, P.: Aerosol remote sensing from POLDER/ADEOS over the ocean: Improved retrieval using a nonspherical particle model, J. Geophys. Res. D Atmos., 110, 1–11, https://doi.org/10.1029/2004JD004798, 2005.

Herrmann, L., Stahr, K., Jahn, R.: The importance of source region identification and their properties for soil-derived dust: The case of Harmattan dust sources for eastern West Africa, Contrib. to Atmos. Phys., 72, 141–150, 1999.

Hoffer, A., Gelencsér, A., Guyon, P., Kiss, G., Schmid, O., Frank, G.P., Artaxo, P., Andreae, M.O.: Optical properties of humic-like substances (HULIS) in biomass-burning aerosols, Atmos. Chem. Phys., 6, 3563–3570, https://doi.org/10.5194/acp-6-3563-2006, 2006.

Jacobson, M.Z.: Isolating nitrated and aromatic aerosols and nitrated aromatic gases as sources of ultraviolet light absorption, J. Geophys. Res. Atmos., 104, 3527–3542, https://doi.org/10.1029/1998JD100054, 1999.

Jickells, T.D., An, Z.S., Andersen, K.K., Baker, A.R., Bergametti, C., Brooks, N., Cao, J.J., Boyd, P.W., Duce, R.A., Hunter, K.A., Kawahata, H., Kubilay, N., LaRoche, J., Liss, P.S., Mahowald, N., Prospero, J.M., Ridgwell, A.J., Tegen, I., Torres, R.: Global iron connections between desert dust, ocean biogeochemistry, and climate, Science, 308, 67–71, https://doi.org/10.1126/science.1105959, 2005.

Journet, E., Balkanski, Y., Harrison, S.P.: A new data set of soil mineralogy for dust-cycle modeling, Atmos. Chem. Phys., 14, 3801–3816, https://doi.org/10.5194/acp-14-3801-2014, 2014.

Kanakidou, M., Seinfeld, J.H., Pandis, S.N., Barnes, I., Dentener, F.J., Facchini, M.C., Van Dingenen, R., Ervens, B., Nenes, A., Nielsen, C.J., Swietlicki, E., Putaud, J.P., Balkanski, Y., Fuzzi, S., Horth, J., Moortgat, G.K., Winterhalter, R., Myhre, C.E.L., Tsigaridis, K., Vignati, E., Stephanou, E.G., Wilson, J.: Organic aerosol and global climate modelling: a review, Atmos. Chem. Phys., 5, 1053–1123, https://doi.org/10.5194/acp-5-1053-2005, 2005.

Kerker, M., Scheiner, P., Cooke, D.D., Kratohvil, J.P.: Absorption index and color of colloidal hematite, J. Colloid Interface Sci., 71, 176–187, https://doi.org/10.1016/0021-9797(79)90231-5, 1979.

Kirchstetter, T.W., Novakov, T., Hobbs, P. V.: Evidence that the spectral dependence of light absorption by aerosols is affected by organic carbon, J. Geophys. Res. Atmos., 109. https://doi.org/10.1029/2004JD004999, 2004.

Koepke, P.: Effective reflectance of oceanic whitecaps, Appl. Opt., 23, 1816, https://doi.org/10.1364/AO.23.001816, 1984.

Koepke, P., Hess, M., Schult, I., Shettle, E.P.: Global Aerosol Data Set, Max-Planck-Institut fur Meteorologie, https://doi.org/ISSN: 0937-1060, 1997.

Koren, I., Kaufman, Y.J.: Direct wind measurements of Saharan dust events from Terra and Aqua satellites, Geophys. Res. Lett., 31, 1–4, https://doi.org/10.1029/2003GL019338, 2004.

Kou, L., Labrie, D., Chylek, P.: Refractive indices of water and ice in the 0.65 to 2.5 μm spectral range, Appl. Opt., 32, 3531, https://doi.org/10.1364/AO.32.003531, 1993.

Koven, C.D. and Fung, I.: Inferring dust composition from wavelength-dependent absorption in Aerosol Robotic Network (AERONET) data, J. Geophys. Res. Atmos., 111, https://doi.org/10.1029/2005JD006678, 2006.

Krueger, B.J., Grassian, V.H., Cowin, J.P., Laskin, A.: Heterogeneous chemistry of individual mineral dust particles from different dust source regions: The importance of particle mineralogy, Atmos. Environ., 38, 6253–6261, https://doi.org/10.1016/j.atmosenv.2004.07.010, 2004.

Atmospheric
Chemistry
and Physics
Discussions

1383 Lafon, S., Rajot, J. L., Alfaro, S. C., Gaudichet, A.: Quantification of iron oxides in desert
1384   aerosol, Atmos. Environ., 38, 1211-1218, 2004.
1385 Lafon, S., Sokolik, I.N., Rajot, J.L., Caquincau, S., Gaudichet, A.: Characterization of iron
1386   oxides in mineral dust aerosols: Implications for light absorption, J. Geophys. Res.
1387   Atmos., 111, 1–19, https://doi.org/10.1029/2005JD007016, 2006.
1388 Laskin, A., Iedema, M. J., Ichkovich, A., Graber, E. R., Taraniuk, I., Rudich, Y.: Direct
1389   observation of completely processed calcium carbonate dust particles, Faraday Discuss.,
1390   130, 453-468, https://doi.org/10.1039/b417366j, 2005.
1391 Lázaro, F.J., Gutiérrez, L., Barrón, V., Gelado, M.D.: The speciation of iron in desert dust
1392   collected in Gran Canaria (Canary Islands): Combined chemical, magnetic and optical
1393   analysis,   Atmos.   Environ.,   42,   8987–8996,
1394   https://doi.org/10.1016/j.atmosenv.2008.09.035, 2008.
1395 Lelieveld, J., Berresheim, H., Borrmann, S., Crutzen, P.J., Dentener, F.J., Fischer, H.,
1396   Feichter, J., Flatau, P.J., Heland, J., Holzinger, R., Korrmann, R., Lawrence, M.G.,
1397   Levin, Z., Markowicz, K.M., Mihalopoulos, N., Minikin, A., Ramanathan, V., De Reus,
1398   M., Roelofs, G.J., Scheeren, H.A., Sciare, J., Schlager, H., Schultz, M., Siegmund, P.,
1399   Steil, B., Stephanou, E.G., Stier, P., Traub, M., Warneke, C., Williams, J., Ziereis, H.:
1400   Global air pollution crossroads over the Mediterranean, Science, 298, 794–799,
1401   https://doi.org/10.1126/science.1075457, 2002.
1402 Léon, J.F. and Legrand, M.: Mineral dust sources in the surroundings of the North Indian
1403   Ocean, Geophys. Res. Lett., 30, https://doi.org/10.1029/2002GL016690, 2003.
1404 Lesins, G., Chylek, P., Lohmann, U.: A study of internal and external mixing scenarios and
1405   its effect on aerosol optical properties and direct radiative forcing, J. Geophys. Res.
1406   Atmos., 107, https://doi.org/10.1029/2001JD000973, 2002.
1407 Levin, Z.: On the interactions of mineral dust, sea-salt particles, and clouds: A measurement
1408   and modeling study from the Mediterranean Israeli Dust Experiment campaign, J.
1409   Geophys. Res., 110, D20202, https://doi.org/10.1029/2005JD005810, 2005.
1410 Levin, Z., Ganor, E., Gladstein, V.: The effects of desert particles coated with sulfate on rain
1411   formation in the Eastern Mediterranean, J. Appl. Meteorol., 35, 1511–1523, 1996.
1412 Li, J., Pósfai, M., Hobbs, P. V., Buseck, P.R.: Individual aerosol particles from biomass
1413   burning in southern Africa: 2, Compositions and aging of inorganic particles, J.
1414   Geophys. Res. Atmos., 108, https://doi.org/10.1029/2002JD002310, 2003.
1415 Li, X. and Strahler, A.H.: Geometric-Optical Bidirectional Reflectance Modeling of the
1416   Discrete Crown Vegetation Canopy: Effect of Crown Shape and Mutual Shadowing,
1417   IEEE Trans. Geosci. Remote Sens., 30, 276–292, https://doi.org/10.1109/36.134078,
1418   1992.
1419 Li, Z., Gu, X., Wang, L., Li, D., Xie, Y., Li, K., Dubovik, O., Schuster, G., Goloub, P.,
1420   Zhang, Y., Li, L., Ma, Y., Xu, H.: Aerosol physical and chemical properties retrieved
1421   from ground-based remote sensing measurements during heavy haze days in Beijing
1422   winter, Atmos. Chem. Phys., 13, 10171–10183, https://doi.org/10.5194/acp-13-10171-
1423   2013, 2013.
1424 Li, Z., Hou, W., Hong, J., Zheng, F., Luo, D., Wang, J., Gu, X., Qiao, Y.: Directional
1425   Polarimetric Camera (DPC): Monitoring aerosol spectral optical properties over land
1426   from satellite observation, J. Quant. Spectrosc. Radiat. Transf., 218, 21–37,
1427   https://doi.org/10.1016/j.jqsrt.2018.07.003, 2018.
1428 Li, Z., Li, L., Zhang, F., Li, D., Xie, Y., Xu, H. : Comparison of aerosol properties over
1429   Beijing and Kanpur: Optical, physical properties and aerosol component composition
1430   retrieved from 12 years ground-based Sun-sky radiometer remote sensing data, J.
1431   Geophys. Res. Atmos., 120, 1520–1535, https://doi.org/10.1002/2014JD022593, 2015.
1432 Liousse, C., Penner, J.E., Chuang, C., Walton, J.J., Eddleman, H., Cachier, H.: A global
1433   three-dimensional model study of carbonaceous aerosols, J. Geophys. Res., 101, 19411–
1434   19432, https://doi.org/10.1029/95JD03426, 1996.
1435 Liu, H., Pinker, R.T., Holben, B.N.: A global view of aerosols from merged transport models,
1436   satellite, and ground observations, J. Geophys. Res. Atmos., 110, 1–16,
1437   https://doi.org/10.1029/2004JD004695, 2005.

Atmospheric
Chemistry
and Physics
Discussions

1438 Longtin, D.R., Shettle, E.P., Hummel, J.R., Pryce, J.D., A Wind Dependent Desert Aerosol
1439   Dust Model: Radiative Properties, Scientific Report No.6, 1988.
1440 Lopatin, A., Dubovik, O., Chaikovsky, A., Goloub, P., Lapyonok, T., Tanré, D., Litvinov, P.:
1441   Enhancement of aerosol characterization using synergy of lidar and Sun- photometer
1442   coincident observations : the GARRLiC algorithm, Atmos. Meas. Tech., 6, 2065–2088,
1443   https://doi.org/10.5194/amt-6-2065-2013, 2013.
1444 Maenhaut, W., Salma, I., Cafmeyer, J., Annegarn, H.J., Andreae, M.O.: Regional atmospheric
1445   aerosol composition and sources in the eastern Transvaal, South Africa, and impact of
1446   biomass burning, J. Geophys. Res., 101, 23631, https://doi.org/10.1029/95JD02930,
1447   1996.
1448 Mahowald, N.M., Baker, A.R., Bergametti, G., Brooks, N., Duce, R.A., Jickells, T.D.,
1449   Kubilay, N., Prospero, J.M., Tegen, I.: Atmospheric global dust cycle and iron inputs to
1450   the ocean. Global Biogeochem, Cycles, 19, https://doi.org/10.1029/2004GB002402,
1451   2005.
1452 Maignan, F., Bréon, F.M., Fédèle, E., Bouvier, M. : Polarized reflectances of natural surfaces:
1453   Spaceborne measurements and analytical modeling, Remote Sens. Environ., 113, 2642–
1454   2650, https://doi.org/10.1016/j.rse.2009.07.022, 2009.
1455 Middleton, N.J.: A geography of dust storms in South-West Asia, J. Climatol., 6, 183–196,
1456   https://doi.org/10.1002/joc.3370060207, 1986a.
1457 Middleton, N.J.: Dust storms in the Middle East, J. Arid Environ., 10, 83–96,
1458   https://doi.org/10.1016/S0140-1963(18)31249-7, 1986b.
1459 Miri, A., Ahmadi, H., Ghanbari, A., Moghaddamnia, A.: Dust Storms Impacts on Air
1460   Pollution and Public Health under Hot and Dry Climate, Int. J. Energy Environ., 2, 101–
1461   105, 2007.
1462 Miyazaki, Y., Kondo, Y., Takegawa, N., Komazaki, Y., Fukuda, M., Kawamura, K.,
1463   Mochida, M., Okuzawa, K., Weber, R.J.: Time-resolved measurements of water-soluble
1464   organic carbon in Tokyo, J. Geophys. Res. Atmos., 111, 1–12,
1465   https://doi.org/10.1029/2006JD007125, 2006.
1466 Orr, C., Hurd, F.K., Corbett, W.J.: Aerosol size and relative humidity, J. Colloid Sci., 13,
1467   472–482, https://doi.org/10.1016/0095-8522(58)90055-2, 1958.
1468 Ota, Y., Higurashi, A., Nakajima, T., Yokota, T.: Matrix formulations of radiative transfer
1469   including the polarization effect in a coupled atmosphere-ocean system, J. Quant.
1470   Spectrosc. Radiat. Transf., 111, 878–894, https://doi.org/10.1016/j.jqsrt.2009.11.021,
1471   2010.
1472 Palmer, K.F. and Williams, D.: Optical properties of water in the near infrared, J. Opt. Soc.
1473   Am., 64, 1107, https://doi.org/10.1364/JOSA.64.001107, 1974.
1474 Popp, T., De Leeuw, G., Bingen, C., Brühl, C., Capelle, V., Chedin, A., Clarisse, L.,
1475   Dubovik, O., Grainger, R., Griesfeller, J., Heckel, A., Kinne, S., Klüser, L., Kosmale,
1476   M., Kolmonen, P., Lelli, L., Litvinov, P., Mei, L., North, P., Pinnock, S., Povey, A.,
1477   Robert, C., Schulz, M., Sogacheva, L., Stebel, K., Zweers, D.S., Thomas, G., Tilstra,
1478   L.G., Vandenbussche, S., Veefkind, P., Vountas, M., Xue, Y.: Development, production
1479   and evaluation of aerosol climate data records from European satellite observations
1480   (Aerosol_cci), Remote Sens., 8, https://doi.org/10.3390/rs8050421, 2016.
1481 Pósfai, M., Simonics, R., Li, J., Hobbs, P. V., Buseck, P.R.: Individual aerosol particles from
1482   biomass burning in southern Africa1: Compositions and size distributions of
1483   carbonaceous particles, J. Geophys. Res. Atmos., 108,
1484   https://doi.org/10.1029/2002JD002291, 2003.
1485 Prospero, J.M., Ginoux, P., Torres, O., Nicholson, S.E., Gill, T.E.: Environmental
1486   characterization of global sources of atmospheric soil dust identified with the Nimbus 7
1487   Total Ozone Mapping Spectrometer (TOMS) absorbing aerosol product, Rev. Geophys.,
1488   40, 1–31, https://doi.org/10.1029/2000RG000095, 2002.
1489 Rashki, A., Rautenbach, C.J. d. W., Eriksson, P.G., Kaskaoutis, D.G., Gupta, P.: Temporal
1490   changes of particulate concentration in the ambient air over the city of Zahedan, Iran,
1491   Air Qual. Atmos. Heal., 6, 123–135, https://doi.org/10.1007/s11869-011-0152-5, 2013.

Reid, J.S., Hobbs, P. V., Ferek, R.J., Blake, D.R., Martins, J.V., Dunlap, M.R., Liousse, C.:
    Physical, chemical, and optical properties of regional hazes dominated by smoke in
    Brazil, J. Geophys. Res. Atmos., 103, 32059–32080,
    https://doi.org/10.1029/98JD00458, 1998.
Román, R., Benavent-oltra, J.A., Casquero-vera, J.A., Lopatin, A., Cazorla, A., Lyamani, H.,
    Denjean, C., Fuertes, D., Perez-Ramirez, D., Torres, B., Toledano, C., Dubovik, O.,
    Cachorro, V.E., de Frutos, A.M., Olmo, F.J., Alados-Arboledas, L.: Retrieval of aerosol
    profiles combining sunphotometer and ceilometer measurements in GRASP code,
    Atmos. Res., 204, 161–177, https://doi.org/10.1016/j.atmosres.2018.01.021, 2018.
Román, R., Torres, B., Fuertes, D., Cachorro, V.E., Dubovik, O., Toledano, C., Cazorla, A.,
    Barreto, A., Frutos, A. De, Alados-arboledas, L.: Remote sensing of lunar aureole with a
    sky camera : Adding information in the nocturnal retrieval of aerosol properties with
    GRASP code, Remote Sens. Environ., 196, 238–252,
    https://doi.org/10.1016/j.rse.2017.05.013, 2017.
Roujean, J.-L., Leroy, M., Deschamps, P.-Y.: A bidirectional reflectance model of the
    Earth's surface for the correction of remote sensing data, J. Geophys. Res., 97, 20455,
    https://doi.org/10.1029/92JD01411, 1992.
Schkolnik, G., Chand, D., Hoffer, A., Andreae, M.O., Erlick, C., Swietlicki, E., Rudich, Y.:
    Constraining the density and complex refractive index of elemental and organic carbon
    in biomass burning aerosol using optical and chemical measurements, Atmos. Environ.,
    41, 1107–1118, https://doi.org/10.1016/j.atmosenv.2006.09.035, 2007.
Schnaiter, M., Gimmler, M., Llamas, I., Linke, C., Jäger, C., Mutschke, H.: Strong spectral
    dependence of light absorption by organic carbon particles formed by propane
    combustion, Atmos. Chem. Phys., 6, 2981–2990, https://doi.org/10.5194/acp-6-2981-
    2006, 2006.
Schuster, G.L., Dubovik, O., Arola, A.: Remote sensing of soot carbon - Part 1:
    Distinguishing different absorbing aerosol species, Atmos. Chem. Phys., 16, 1565–
    1585, https://doi.org/10.5194/acp-16-1565-2016, 2016.
Schuster, G.L., Dubovik, O., Holben, B.N., Clothiaux, E.E.: Inferring black carbon content
    and specific absorption from Aerosol Robotic Network (AERONET) aerosol retrievals,
    J. Geophys. Res., 110, D10S17, https://doi.org/10.1029/2004JD004548, 2005.
Schuster, G.L., Lin, B., Dubovik, O.: Remote sensing of aerosol water uptake, Geophys. Res.
    Lett., 36, https://doi.org/10.1029/2008GL036576, 2009.
Shi, Z., Krom, M.D., Jickells, T.D., Bonneville, S., Carslaw, K.S., Mihalopoulos, N., Baker,
    A.R., Benning, L.G.: Impacts on iron solubility in the mineral dust by processes in the
    source region and the atmosphere: A review, Aeolian Res., 5, 21–42,
    https://doi.org/10.1016/j.aeolia.2012.03.001, 2012.
Sokolik, I.N. and Toon, O.B.: Incorporation of mineralogical composition into models of the
    radiative properties of mineral aerosol from UV to IR wavelengths, J. Geophys. Res.
    Atmos., 104, 9423–9444, https://doi.org/10.1029/1998JD200048, 1999.
Stone, E., Schauer, J., Quraishi, T.A., Mahmood, A. : Chemical characterization and source
    apportionment of fine and coarse particulate matter in Lahore, Pakistan, Atmos.
    Environ., 44, 1062–1070, https://doi.org/10.1016/j.atmosenv.2009.12.015, 2010.
Streets, D.G., Gupta, S., Waldhoff, S.T., Wang, M.Q., Bond, T.C., Yiyun, B.: Black carbon
    emissions in China, Atmos. Environ., 35, 4281–4296, https://doi.org/10.1016/S1352-
    2310(01)00179-0, 2001.
Sun, H., Biedermann, L., Bond, T.C.: Color of brown carbon: A model for ultraviolet and
    visible light absorption by organic carbon aerosol, Geophys. Res. Lett., 34,
    https://doi.org/10.1029/2007GL029797, 2007.
Swap, R., Garstang, M., Macko, S.A., Tyson, P.D., Maenhaut, W., Artaxo, P., Kållberg, P.,
    Talbot, R.: The long-range transport of southern African aerosols to the tropical South
    Atlantic, J. Geophys. Res. Atmos., 101, 23777–23791,
    https://doi.org/10.1029/95JD01049, 1996.
Tang, I.N.: Chemical and size effects of hygroscopic aerosols on light scattering coefficients,
    J. Geophys. Res. Atmos., 101, 19245–19250, https://doi.org/10.1029/96JD03003, 1996.

1547 Tang, I.N.: Phase transformation and growth of aerosol particles composed of mixed salts, J.
1548   Aerosol Sci., 7361–7371, https://doi.org/10.1016/0021-8502(76)90022-7, 1976.
1549 Tang, I.N. and Munkelwitz, H.R.: Water activities, densities, and refractive indices of
1550   aqueous sulfates and sodium nitrate droplets of atmospheric importance 99, 18801–
1551   18808, 1994.
1552 Tang, I.N. and Munkelwitz, H.R.: Composition and temperature dependence of the
1553   deliquescence properties of hygroscopic aerosols, Atmos. Environ., 27, 467–473,
1554   https://doi.org/10.1016/0960-1686(93)90204-C, 1993.
1555 Tang, I.N. and Munkelwitz, H.R.: Simultaneous determination of refractive index and density
1556   of an evaporating aqueous solution droplet, Aerosol Sci. Technol., 15, 201–207,
1557   https://doi.org/10.1080/02786829108959527, 1991.
1558 Tanré, D., Bräon, F.M., Deuzä, J.L., Dubovik, O., Ducos, F., Franäois, P., Goloub, P.,
1559   Herman, M., Lifermann, A., Waquet, F.: Remote sensing of aerosols by using polarized,
1560   directional and spectral measurements within the A-Train: The PARASOL mission,
1561   Atmos. Meas. Tech., 4, 1383–1395, https://doi.org/10.5194/amt-4-1383-2011, 2011.
1562 Todd, M.C., Washington, R., Martins, J.V., Dubovik, O., Lizcano, G., M'Bainayel, S.,
1563   Engelstaedter, S.: Mineral dust emission from the Bodélé Depression nothern Chad,
1564   during BoDEx 2005, J. Geophys. Res. Atmos., 112, 1–12,
1565   https://doi.org/10.1029/2006JD007170, 2007.
1566 Triaud, A.H.M.J.: Earth observation data group: aerosol refractive index archive.
1567   http://eodg.atm.ox.ac.uk/ARIA/data?Minerals/Hematite/(Triaud_2005)/hematite_Triaud
1568   _2005.ri, 2005.
1569 Tsekeri, A., Lopatin, A., Amiridis, V., Marinou, E., Igloffstein, J., Siomos, N., Solomos, S.,
1570   Kokkalis, P., Engelmann, R., Baars, H., Gratsea, M., Raptis, P.I.: GARRLiC and
1571   LIRIC : strengths and limitations for the characterization of dust and marine particles
1572   along with their mixtures, Atmos. Meas. Tech., 10, 4995–5016,
1573   https://doi.org/10.5194/amt-10-4995-2017, 2017.
1574 Usher, C. R., Michel, A. E., Grassian, V. H.: Reactions on mineral dust, Chem. Rev., 103,
1575   4883-4939, https://doi.org/10.1021/cr020657y, 2003.
1576 Voss, K.J., Morel, A., Antoine, D.: Detailed validation of the bidirectional effect in various
1577   Case 1 waters for application to ocean color imagery, Biogeosciences, 4, 781–789,
1578   https://doi.org/10.5194/bg-4-781-2007, 2007
1579 Wang, L., Li, Z., Tian, Q., Ma, Y., Zhang, F., Zhang, Y., Li, D., Li, K., Li, L. : Estimate of
1580   aerosol absorbing components of black carbon, brown carbon, and dust from ground-
1581   based remote sensing data of sun-sky radiometers, J. Geophys. Res. Atmos., 118, 6534–
1582   6543, https://doi.org/10.1002/jgrd.50356, 2013.
1583 Wanner, W., Li, X., Strahler, A. : On the derivation of kernels for kernel-driven models of
1584   bidirectional reflectance, J. Geophys. Res., 100, 21077–21089, 1995.
1585 Waquet, F., Cornet, C., Deuzé, J.L., Dubovik, O., Ducos, F., Goloub, P., Herman, M.,
1586   Lapyonok, T., Labonnote, L.C., Riedi, J., Tanré, D., Thieuleux, F., Vanbauce, C.:
1587   Retrieval of aerosol microphysical and optical properties above liquid clouds from
1588   POLDER/PARASOL polarization measurements, Atmos. Meas. Tech., 6, 991–1016,
1589   https://doi.org/10.5194/amt-6-991-2013, 2013.
1590 Washington, R., Todd, M., Middleton, N.J., Goudie, A.S.: Dust-storm source areas
1591   determined by the total ozone monitoring spectrometer and surface observations, Ann.
1592   Assoc. Am. Geogr., 93, 297–313, https://doi.org/10.1111/1467-8306.9302003, 2003.
1593 Washington, R. and Todd, M.C.: Atmospheric controls on mineral dust emission from the
1594   Bodélé Depression, Chad: The role of the low level jet, Geophys. Res. Lett., 32, 1–5.
1595   https://doi.org/10.1029/2005GL023597, 2005.
1596 Washington, R., Todd, M.C., Engelstaedter, S., Mbainayel, S., Mitchell, F.: Dust and the low-
1597   level circulation over the Bodélé Depression, Chad: Observations from BoDEx 2005, J.
1598   Geophys. Res. Atmos., 111, 1–15, https://doi.org/10.1029/2005JD006502, 2006.
1599 Weber, R.J., Sullivan, A.P., Peltier, R.E., Russell, A., Yan, B., Zheng, M., de Grouw, J.,
1600   Warneke, C., Brock, C., Holloway, J.S., Atlas, E.L., Edgerton, E.: A study of secondary
1601   organic aerosol formation in the anthropogenic-influenced southeastern United States, J.

Atmospheric
Chemistry
and Physics
Discussions
Open Access
EGU

1602 Geophys. Res. Atmos., 112, 1–13, https://doi.org/10.1029/2007JD008408, 2007.
1603 Yu, H., Dickinson, R.E., Chin, M., Kaufman, Y.J., Holben, B.N., Geogdzhayev, I. V.,
1604 Mishchenko, M.I.: Annual cycle of global distributions of aerosol optical depth from
1605 integration of MODIS retrievals and GOCART model simulations, J. Geophys. Res.
1606 Atmos., 108, 1–14, https://doi.org/10.1029/2002JD002717, 2003
1607 Yu, H., Dickinson, R.E., Chin, M., Kaufman, Y.J., Zhou, M., Zhou, L., Tian, Y., Dubovik,
1608 O., Holben, B.N.: Direct radiative effect of aerosols as determined from a combination
1609 of MODIS retrievals and GOCART simulations, J. Geophys. Res. Atmos., 109, 1–13,
1610 https://doi.org/10.1029/2003JD003914, 2004.
1611 Yu, H., Kaufman, Y.J., Chin, M., Feingold, G., Remer, L.A., Anderson, T.L., Balkanski, Y.,
1612 Bellouin, N., Boucher, O., Christopher, S., DeCola, P., Kahn, R., Koch, D., Loeb, N.,
1613 Reddy, M.S., Schulz, M., Takemura, T., Zhou, M.: A review of measurement-based
1614 assessments of the aerosol direct radiative effect and forcing, Atmos. Chem. Phys., 6,
1615 613–666, https://doi.org/10.5194/acp-6-613-2006, 2006.
1616 Zhang, X. Y., Gong, S. L., Shen, Z. X., Mei, F. M., Xi, X. X., Liu, L. C., Zhou, Z. J., Wang,
1617 D., Wang, Y. Q., Cheng, Y.: Characterization of soil dust aerosol in China and its
1618 transport and distribution during 2001 ACE-Asia: 1. Network observations, J. Geophys.
1619 Res., 108 (D9), 4261, https://doi.org/4210.1029/2002JD002632, 2003.
1620 Zhang, J., Reid, J.S., Westphal, D.L., Baker, N.L., Hyer, E.J.: A system for operational
1621 aerosol optical depth data assimilation over global oceans, J. Geophys. Res. Atmos.,
1622 113, 1–13, https://doi.org/10.1029/2007JD009065, 2008a.
1623 Zhang, X.Y., Wang, Y.Q., Niu, T., Zhang, X.C., Gong, S.L., Zhang, Y.M., Sun, J.Y.:
1624 Atmospheric aerosol compositions in China: Spatial/temporal variability, chemical
1625 signature, regional haze distribution and comparisons with global aerosols, Atmos.
1626 Chem. Phys., 12, 779–799, https://doi.org/10.5194/acp-12-779-2012, 2012.
1627 Zhang, X.Y., Wang, Y.Q., Wang, D., Gong, S.L., Arimoto, R., Mao, L.J., Li, J.:
1628 Characterization and sources of regional-scale transported carbonaceous and dust
1629 aerosols from different pathways in coastal and sandy land areas of China, J. Geophys.
1630 Res. Atmos., 110, 1–13, https://doi.org/10.1029/2004JD005457, 2005.
1631 Zhang, X.Y., Wang, Y.Q., Zhang, X.C., Guo, W., Gong, S.L.: Carbonaceous aerosol
1632 composition over various regions of China during 2006, J. Geophys. Res. Atmos., 113,
1633 1–10, https://doi.org/10.1029/2007JD009525, 2008b.
1634
1635
1636
1637
1638
1639
1640
1641
1642
1643
1644
1645
1646
1647
1648
1649
1650
1651
1652
1653
1654

1655
1656 **Tables**
1657
1658
1659 **Table 1**. List of measured and retrieved characteristic considered in POLDER/GRASP with
1660 aerosol composition mixing model. $\mu_0 = cos(\vartheta_0)$ depends on the solar zenith angle ϑ_0,
1661 $\mu_1 = cos(\vartheta_1)$ depends on the observation zenith angle ϑ_1. φ_0 and φ_1 represent the solar and
1662 observation azimuth angles.
1663

POLDER/PARASOL measurements	
Measurements type:	
$I(\mu_0; \mu_1; \varphi_0; \varphi_1; \lambda_i) = I(\Theta_j; \lambda_i)$	– I reflected total radiances
$Q(\mu_0; \mu_1; \varphi_0; \varphi_1; \lambda_i) = Q(\Theta_j; \lambda_i)$	– Q component of the Stokes vector
$U(\mu_0; \mu_1; \varphi_0; \varphi_1; \lambda_i) = U(\Theta_j; \lambda_i)$	– U component of the Stokes vector
Observation specifications:	
Angular:	
	$I(\Theta_j; \lambda_i), Q(\Theta_j; \lambda_i)$ and $U(\Theta_j; \lambda_i)$ measured in up to 16 viewing directions, that may cover the range of scattering angle Θ from ~ 80° to 180°
Spectral:	
	$I(\Theta_j; \lambda_i)$ measured in 6 window channels $\lambda_i =$ 0.440, 0.490, 0.565, 0.670, 0.865 and 1.02 μm
	$Q(\Theta_j; \lambda_i)$ and $U(\Theta_j; \lambda_i)$ measured in 3 window channels $\lambda_i =$ 0.490, 0.670, and 0.865 μm
Retrieved characteristic	
Aerosol parameters:	
C_v	– total volume concentration of aerosol ($\mu m^3/\mu m^2$)
$dV(r_i)/dlnr$	– ($i = 1, ..., N_r$) values of volume size distribution in N_i size bins r_i normalized by C_v
C_{sph}	– fraction of spherical particles
h_0	– mean height of aerosol layer
$Frac(F_i)$	– ($i = 1, ..., N_f$) the fraction of composition in fine mode
$Frac(C_i)$	– ($i = 1, ..., N_c$) the fraction of composition in coarse mode
Surface reflection parameters:	
Ross-Li model parameters:	
$k_{iso}(\lambda_i)$	– ($i = 1, ..., N_\lambda = 6$) first Ross-Li model parameter (isotropic parameter characterizing isotropic surface reflectance)
$k_{vol}(\lambda_i)$	– ($i = 1, ..., N_\lambda = 6$) second Ross-Li model parameter (volumetric parameter characterizing anisotropy of reflectance)
$k_{geom}(\lambda_i)$	– ($i = 1, ..., N_\lambda = 6$) third Ross-Li model parameter (geometric parameter characterizing anisotropy of reflectance)
Maignan et al. (2009) model:	
$B(\lambda_i)$	– ($i = 1, ..., N_\lambda = 6$) free parameter

1664
1665
1666
1667
1668

Atmospheric
Chemistry
and Physics
Discussions

Table 2. List of statistics for parameters between assumed and retrieved in the sensitivity tests of GRASP composition retrieval using Maxwell-Garnett mixing model. The values of slope (A), intercept (B), correlation coefficient (R), root-mean-square error (RMSE), mean absolute error (MEA), mean relative error (MRE) and standard error deviation (STD) are presented for aerosol compositions, aerosol optical thickness (AOT), Single-scattering albedo (SSA), real (n) and imaginary (k) parts of complex refractive index in fine mode (FM) and coarse mode (CM) at 675 nm.

	A	B	R	RMSE	MAE	MRE	STD
BC	1.00	0.00	1.00	0.00	0.00	0.4%	0.00
BrC	1.00	0.00	1.00	0.00	0.00	2.7%	0.00
FNAI	1.02	-0.02	0.99	0.03	-0.01	-1.0%	0.03
FNAS	1.03	-0.03	1.00	0.01	-0.02	-6.0%	0.01
FAWC	0.99	0.00	1.00	0.02	0.00	-0.2%	0.02
RH	0.94	0.04	0.97	0.03	0.00	0.3%	0.03
CAI	1.00	0.00	1.00	0.00	0.00	-1.1%	0.00
CNAI	0.95	0.01	0.99	0.02	0.00	8.2%	0.02
CNAS	0.95	0.00	1.00	0.01	-0.02	-4.5%	0.01
CAWC	1.01	0.00	1.00	0.02	0.00	0.9%	0.02
AOT	1.00	0.00	1.00	0.00	0.00	0.0%	0.00
SSA	1.00	0.00	1.00	0.00	0.00	0.0%	0.00
FM(n)	0.98	0.03	1.00	0.00	0.00	0.1%	0.00
FM(k)	1.00	0.00	1.00	0.0003	0.0001	0.5%	0.00
CM(n)	1.00	0.00	1.00	0.00	0.00	0.0%	0.00
CM(k)	0.96	0.00	1.00	0.0000	0.0000	5.8%	0.00

Table 3. The statistics of aerosol parameters in Fig. 10: number of measurements (N), slope (A), intercept (B), correlation coefficient (R), root-mean-square error (RMSE), mean absolute error (MAE), standard error deviation (STD). GRASP approach (GA): Maxwell-Garnett (MG) mixing model, volume-weighted (VW) mixing model; standard (ST) GRASP/PARASOL retrievals without aerosol composition mixing model.

	Banizoumbou AOT (675 nm)			Tamanrasset AOT (675 nm)			Mongu AOT (675 nm)		
N	78			76			118		
GA	MG	VW	ST	MG	VW	ST	MG	VW	ST
A	0.75	0.96	0.68	0.68	0.88	0.49	0.90	0.96	0.96
B	-0.02	-0.05	0.08	0.03	0.06	0.13	-0.01	0.00	0.00
R	0.97	0.96	0.91	0.89	0.88	0.51	0.96	0.95	0.94
RMSE	0.08	0.11	0.13	0.05	0.07	0.12	0.04	0.05	0.06
MAE	-0.15	-0.07	-0.08	-0.02	0.04	0.05	-0.04	-0.01	-0.01
STD	0.13	0.11	0.19	0.07	0.07	0.14	0.05	0.05	0.06

	Skukuza AOT (675 nm)			Solar village AOT (675 nm)			Agoufou AOT (675 nm)		
N	92			98			117		
GA	MG	VW	ST	MG	VW	ST	MG	VW	ST
A	0.83	0.96	0.89	0.75	0.83	0.67	0.83	0.98	0.72
B	-0.01	0.00	0.01	0.00	0.02	0.10	0.00	0.00	0.20
R	0.79	0.76	0.84	0.91	0.91	0.79	0.94	0.94	0.84
RMSE	0.05	0.06	0.04	0.09	0.10	0.13	0.14	0.16	0.21
MAE	-0.03	-0.01	-0.01	-0.11	-0.06	-0.05	-0.10	-0.01	0.04
STD	0.05	0.06	0.04	0.11	0.11	0.16	0.16	0.16	0.25

	All sites AOT (675 nm)			All sites AE (870/440)			All sites SSA (675 nm)		
N	579			429			101		
GA	MG	VW	ST	MG	VW	ST	MG	VW	ST
A	0.79	0.93	0.77	0.86	0.79	0.88	0.57	0.59	0.65
B	0.00	0.00	0.07	0.20	0.17	0.16	0.44	0.42	0.32
R	0.95	0.95	0.88	0.93	0.92	0.94	0.83	0.84	0.77
RMSE	0.09	0.11	0.15	0.24	0.24	0.24	0.02	0.02	0.03
MAE	-0.07	-0.02	-0.01	0.08	0.00	0.06	0.04	0.04	0.00
STD	0.11	0.11	0.17	0.26	0.29	0.25	0.03	0.03	0.04

1717
1718 **Figures**
1719
1720
1721

General structure of inversion algorithm
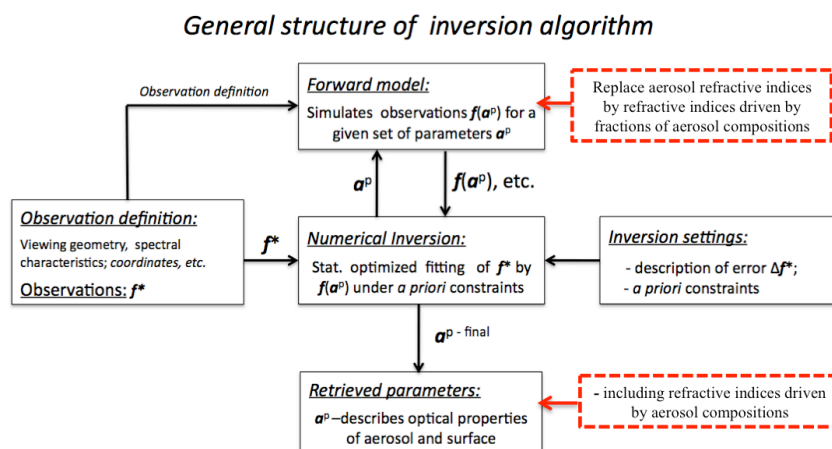
1722
1723 **Figure 1.** The general structure of GRASP algorithm with aerosol composition conversion
1724 model, courtesy of (Dubovik et al., 2011). The red dashed frames represent modifications
1725 for the composition inversion approach. f^* represents vector of inverted measurements, a^P
1726 represents vector of unknowns at the p-th iteration, $f(a^P)$ represents vector of measurement
1727 fit at the p-th iteration.
1728
1729
1730
1731
1732
1733
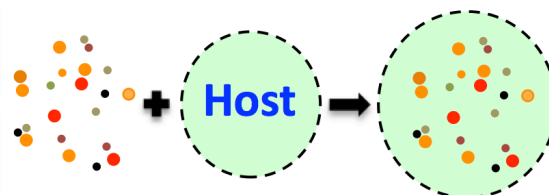
1734
1735 **Figure 2.** Illustrates a general logistics of an effective refractive index calculation using a
1736 conversion model that is based upon the Maxwell-Garnett effective medium approximation.
1737
1738

Atmospheric
Chemistry
and Physics
Discussions
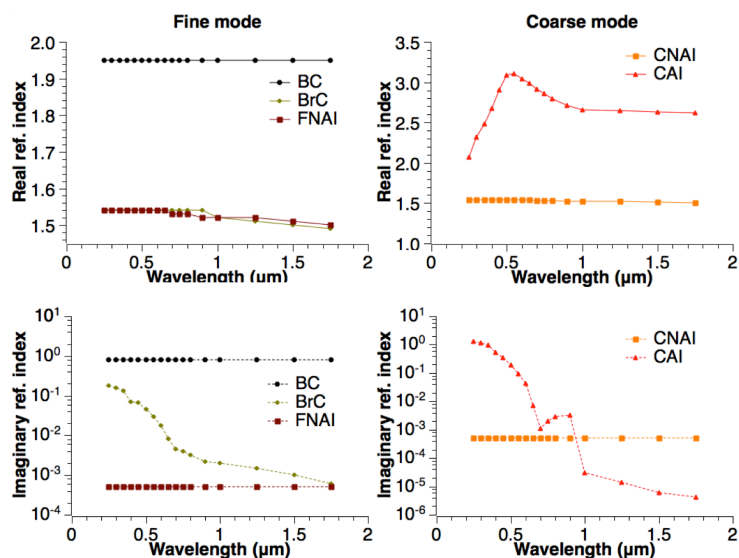
Figure 3. The refractive indices of assumed aerosol compositions embedded in the host of the size-dependent Maxwell-Garnett conversion model. The parameters of BC refer to Bond and Bergstrom (2006). The parameters of BrC refer to Sun et al. (2007) and Schuster et al. (2016). The parameters of fine non-absorbing insoluble (FNAI) and coarse non-absorbing insoluble (CNAI) refer to Ghosh (1999). FNAI represents dust and OC in fine mode particles, while CNAI represents dust in coarse mode particles. The parameters of coarse absorbing insoluble (CAI) refer to Longtin et al. (1988) representing hematite.
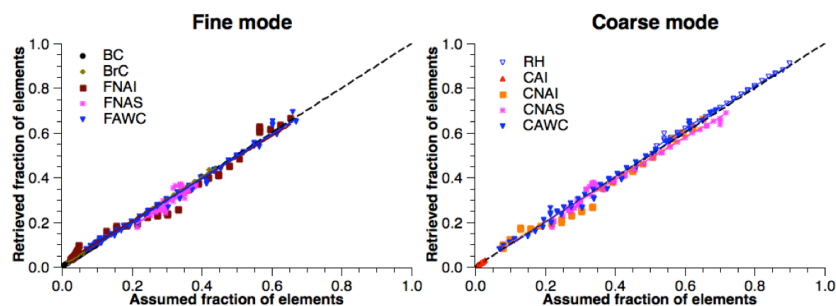
Figure 4. Assumed and retrieved fractions of aerosol composition species resulting from the sensitivity tests of GRASP composition retrieval using Maxwell-Garnett mixing model.

Atmospheric
Chemistry
and Physics
Discussions
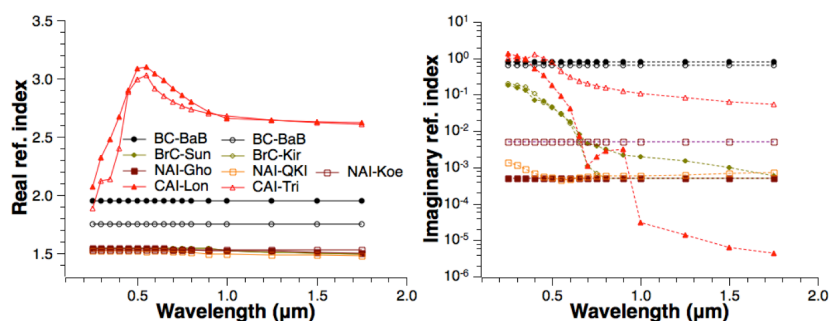
Figure 5. Complex refractive index of several aerosol species (BC, BrC, CAI, and NAI) in the host. The values with filled symbols are used in the presented size-dependent Maxwell-Garnett conversion model. The values with open symbols are used to replace the corresponding values to test the uncertainties in the aerosol composition retrievals. "BaB" for Bond and Bergstrom (2006); "Sun" for Sun et al. (2007); "Kir" for Kirchstetter et al. (2004); "Gho" for Ghosh (1999); "QKI" for dust composed of a mixture of quartz (Ghosh, 1999), kaolinite (Sokolik and Toon, 1999) and illite (Sokolik and Toon, 1999) with the proportions of 48%, 26%, and 26%, respectively (Journet et al., 2014); "Koe" for Koepke et al. (1997); "Lon" for Longtin et al. (1988); and "Tri" for Triaud (2005).
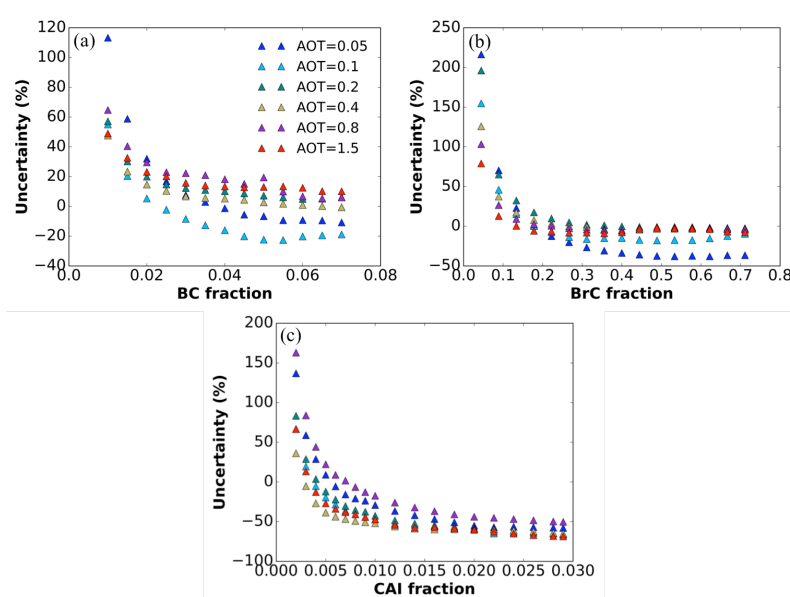
Figure 6. Uncertainty in absorbing species retrievals from POLDER/PARASOL attributed to the refractive index variability; uncertainties in (a) BC, (b) BrC, and (c) CAI fractions.

Atmospheric
Chemistry
and Physics
Discussions
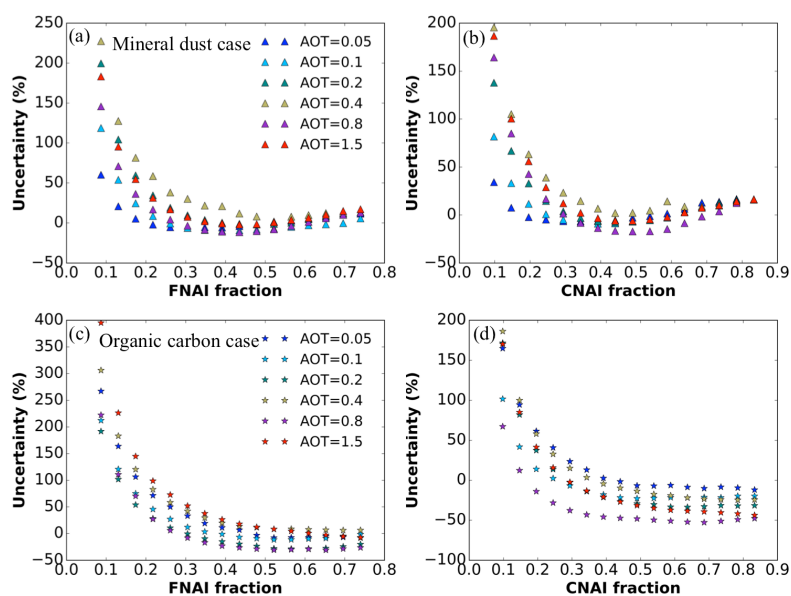
Figure 7. Uncertainty in Non-Absorbing Insoluble particles fraction in Fine (FNAI) and Coarse (CNAI) modes attributed to the refractive index variability: (a), (b) for the case of mineral dust and (c), (d) for organic carbon.
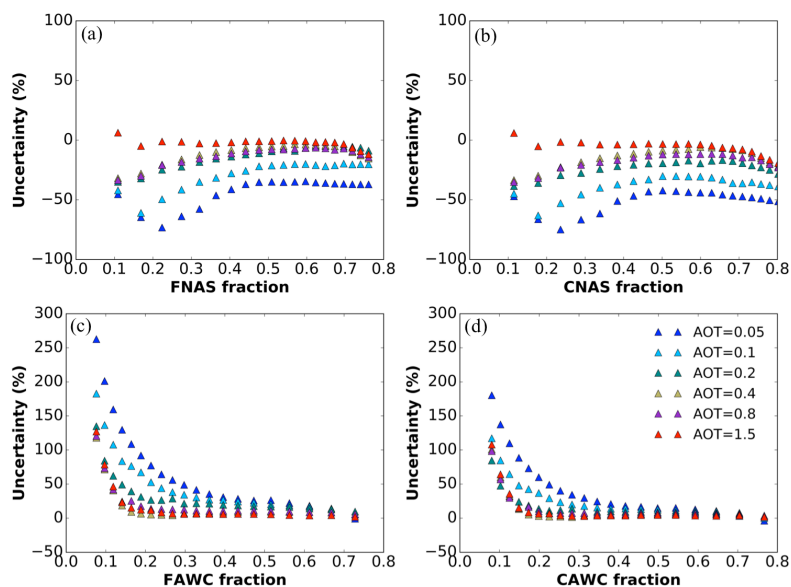
Figure 8. Uncertainty in Non-Absorbing Soluble particles and aerosol water content fraction in Fine (FNAS, FAWC) and Coarse (CNAS, CAWC) modes attributed to the refractive index and hygroscopic properties of ammonium nitrate and ammonium sulfate.

1786
1787
1788
1789
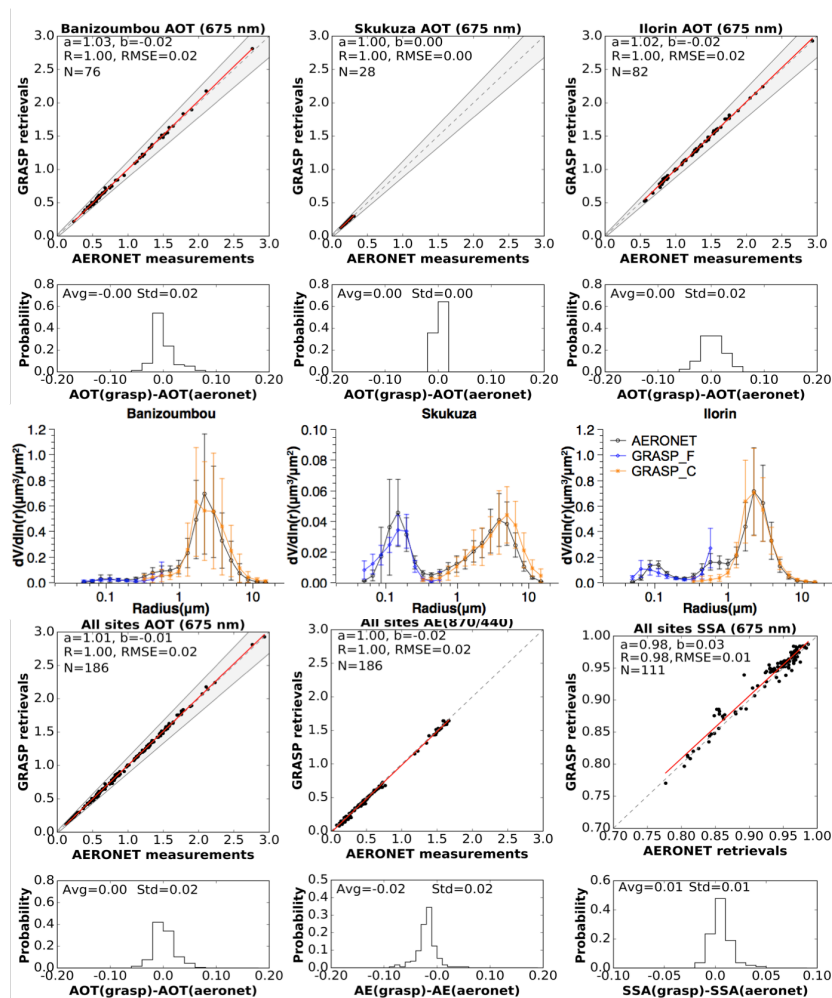
1790
1791
1792 **Figure 9.** The inter-comparison of aerosol optical properties derived from Sun/sky
1793 photometer measurements using the GRASP/Composition approach with the corresponding
1794 values of the AERONET operational product. The data presented for the Banizoumbou site in
1795 April 2007 represent mineral dust aerosol, for the Skukuza site in September 2007 represent
1796 the biomass burning aerosol, and for the Ilorin site in January 2007 represent the mixture of
1797 dust and biomass burning.
1798
1799
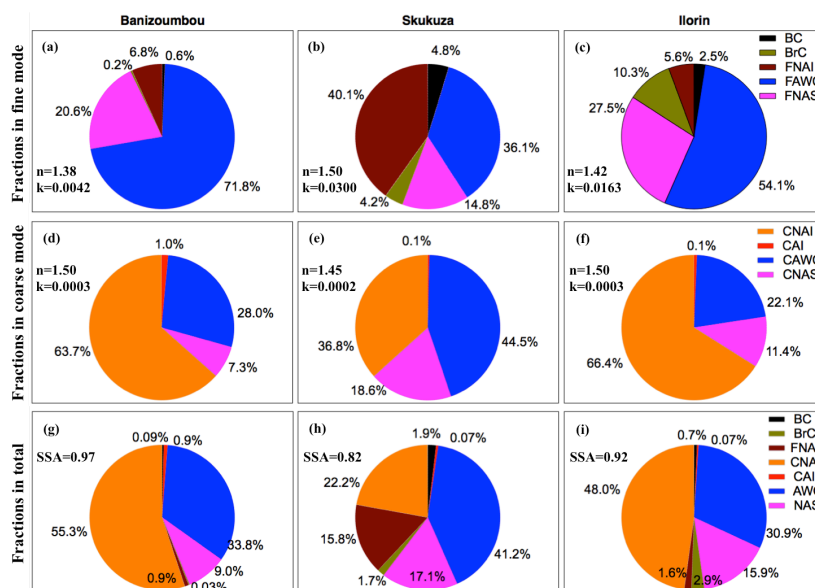
Figure 10. Examples of aerosol composition retrievals derived from AERONET Sun/sky photometer measurements using the GRASP/Composition approach. Panels: (a, d, g) the mineral dust case at the Banizoumbou site (April 8th, 2007); (b, e, h) the biomass burning case at the Skukuza site (September 2nd, 2007); and (c, f, i) the mixture of dust and biomass burning at the Ilorin site (January 25th, 2007). In the panes are also indicated the values of complex refractive index (n, k) at 675 nm retrieved for the fine and coarse modes, and of SSA at 675 nm derived for ensemble of aerosol.
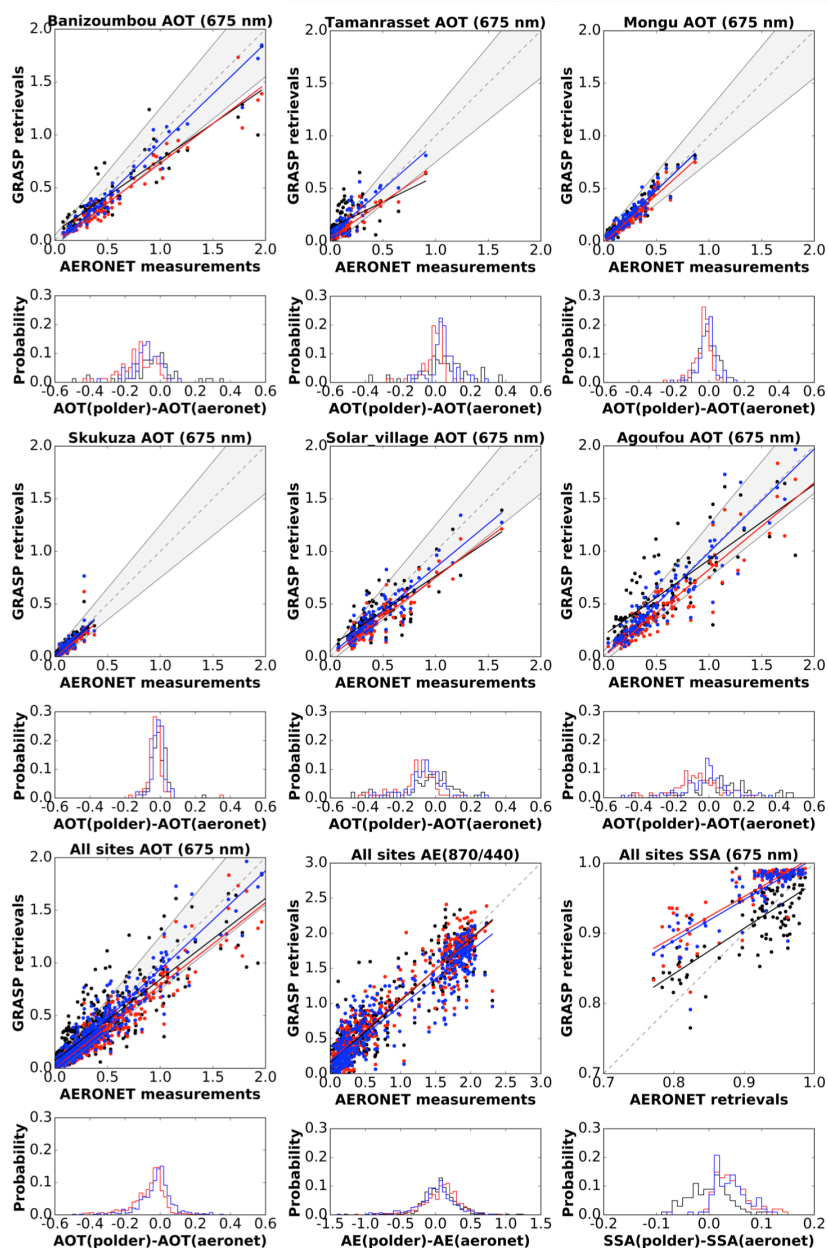
Figure 11. Inter-comparison of aerosol optical properties retrieved from POLDER/PARASOL and provided by AERONET operational product in six AERONET sites located in Africa and Middle East during the period 2006 to 2008. Red color represents the Maxwell-Garnett (MG) mixing model; blue color represents the volume-weighted (VW) mixing model; and black color represents the standard (ST) GRASP/PARASOL product that do not employ the aerosol composition retrievals.

1818
1819
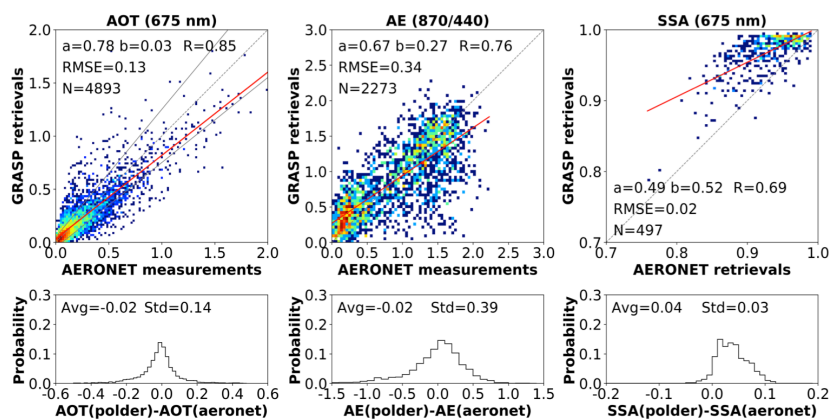
1820
1821 **Figure 12.** Inter-comparison of aerosol optical properties retrieved using the
1822 POLDER/PARASOL composition (MG mixing model) approach and the corresponding
1823 operational AERONET products from all globally available sites in 2008.

1824

1825

1826

1827
1828 **Figure 13**. Seasonal variability of number of pixels in 0.1×0.1 degree resolution observed by
1829 POLDER/PARASOL satellite over the globe in 2008.
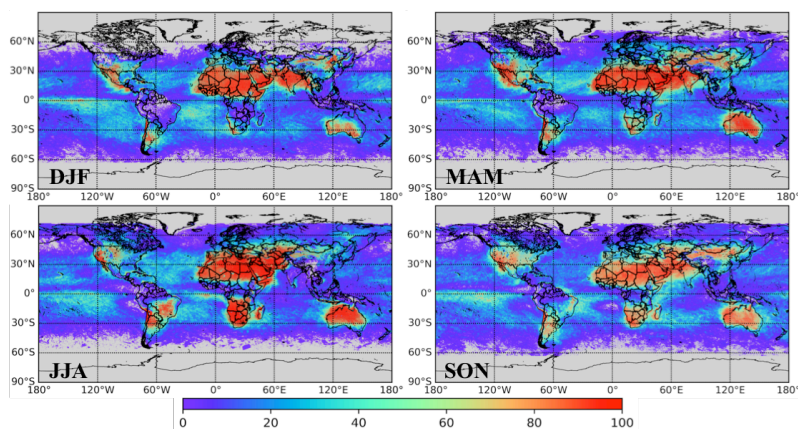
1830
1831
1832
1833
1834
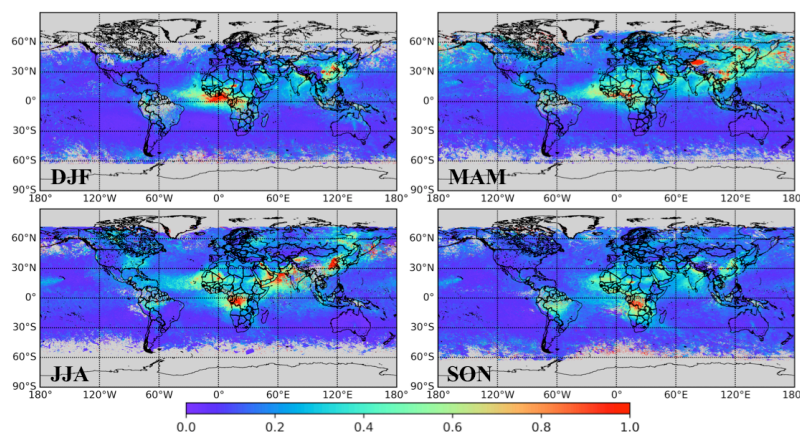
Figure 14. Seasonal variability of AOT at 565 nm in 2008 as retrieved by GRASP/Composition algorithm from POLDER/PARASOL satellite observations.
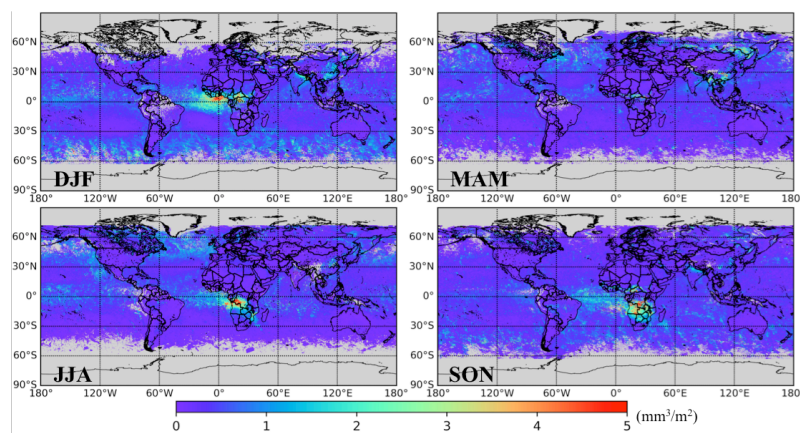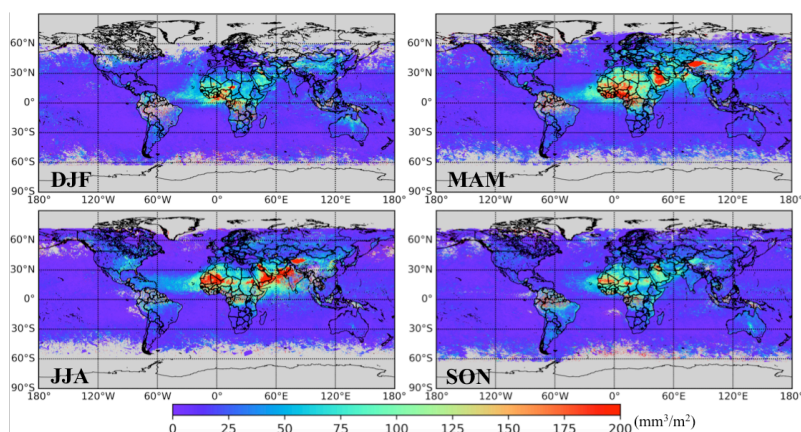

Figure 15. Seasonal variability of BC column volume concentration (mm^3/m^2) over the globe in 2008 as retrieved by GRASP/Composition algorithm from POLDER/PARASOL satellite observations.
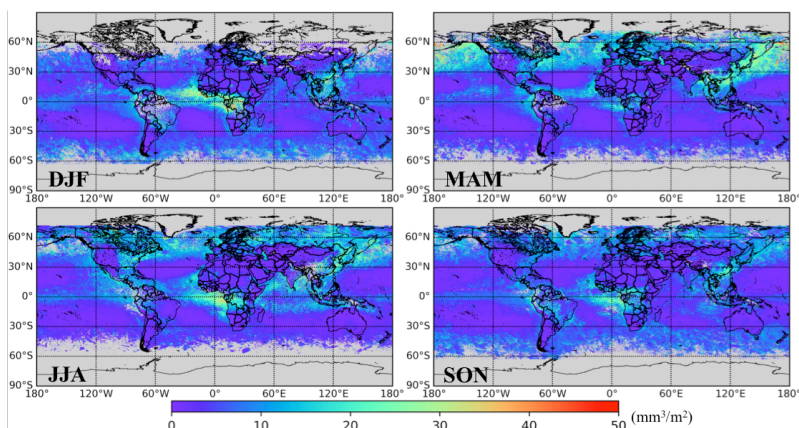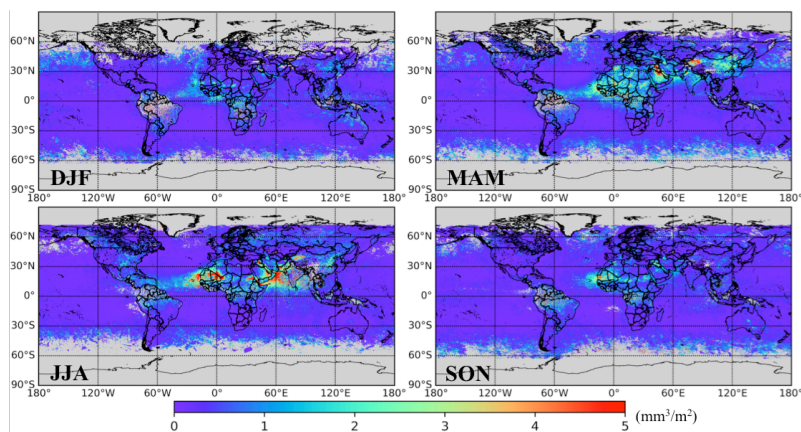
Figure 16. Same as Fig. 15, but for BrC
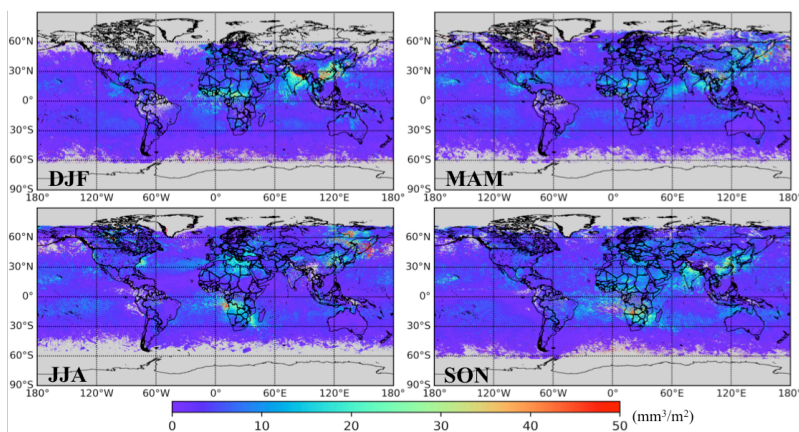
Figure 17. Same as Fig. 15, but for fine mode non-absorbing soluble (FNAS)
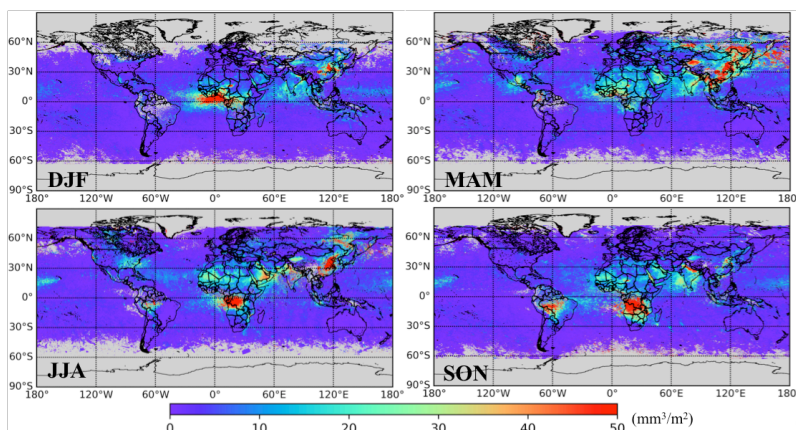
1867
1868   **Figure 18**. Same as Fig. 15, but for coarse mode non-absorbing insoluble (CNAI, dust)
1869
1870
1871
1872
1873

1874
1875   **Figure 19**. Same as Fig. 15, but for coarse mode absorbing insoluble (CAI, FeOx and
1876   Carbonaceous)
1877
1878
1879
1880

Figure 20. Same as Fig. 15, but for fine mode non-absorbing insoluble (FNAI, dust and OC)